The Electrochemical Society
Advancing solid state & electrochemical science & technology

Operando Identification of Liquid Intermediates in Lithium–Sulfur Batteries via Transmission UV–vis Spectroscopy

CrossMark

Operando Identification of Liquid Intermediates in Lithium–Sulfur Batteries via Transmission UV–vis Spectroscopy

Qi He,[a,z] Anna T. S. Freiberg,* Manu U. M. Patel,[b] Simon Qian,* and Hubert A. Gasteiger**

Chair of Technical Electrochemistry, Department of Chemistry and Catalysis Research Center, Technical University of Munich, D-85748 Garching, Germany

Lithium-sulfur (Li-S) batteries are facing various challenges with regards to performance and durability, and further improvements require a better understanding of the fundamental working mechanisms, including an identification of the reaction intermediates in an operating Li-S battery. In this study, we present an *operando* transmission UV–vis spectro-electrochemical cell design that employs a conventional sulfur/carbon composite electrode, propose a comprehensive peak assignment for polysulfides in DOL: DME-based electrolyte, and finally identify the liquid intermediates in the discharging process of an operating Li-S cell. Here, we propose for the first time a meta-stable polysulfide species (S_3^{2-}) that is present at substantial concentrations during the 2nd discharge plateau in a Li-S battery. We identify the S_3^{2-} species that are the reduction product of S_4^{2-}, as deducted from the analysis of the obtained *operando* UV–vis spectra along with the transferred charge, and confirmed by rotating ring disk electrode measurements for the reduction of a solution with a nominal Li_2S_4 stoichiometry. Furthermore, our *operando* results provide insight into the potential-dependent stability of different S-species and the rate-limiting (electro)chemical steps during discharging. Finally, we propose a viable reaction pathway of how S_8 is electrochemically reduced to Li_2S_2/Li_2S based on our *operando* results as well as that reported in the literature.

As one of the most important strategies to move the world's energy landscape toward clean, renewable energy, lithium-ion batteries (Li-ion, based on intercalation electrochemistry) have been intensively developed and widely commercialized. Despite the significant improvement in increasing the energy density over the years, there is a growing consensus that current Li-ion batteries might be unable to satisfy the requirements of future technologies.[1] In the search for high energy density and inexpensive post Li-ion batteries, the lithium-sulfur battery system (Li-S, based on conversion electrochemistry) has attracted tremendous attention worldwide due to its high theoretical specific capacity (1675 mAh/g_{sulfur}) as well as due to the high natural abundance and non-toxicity of elemental sulfur.[1–8]

The reversible conversion (Eq. 1) between elemental sulfur (S_8) and lithium sulfide (Li_2S) is believed to be accompanied by a series of soluble reaction intermediates, namely polysulfides (Li_2S_x; x referring to the total possible range of S atoms), in liquid electrolyte Li-S batteries. It is general believed that reduction of S_8 first generates long-chain polysulfides (Li_2S_n, here defined to be $5 \leqslant n \leqslant 8$), that can be further reduced to short-chain polysulfides (Li_2S_m, here defined to be $2 \leqslant m \leqslant 4$), and eventually the solid product Li_2S is formed[1,6,7,9–12]:

$$S_8 + 16e^- + 16Li^+ \leftrightarrow \frac{8}{n}Li_2S_n + aLi^+ + ae^- \leftrightarrow \frac{8}{m}Li_2S_m$$
$$+ bLi^+ + be^- \leftrightarrow 8Li_2S \qquad [1]$$
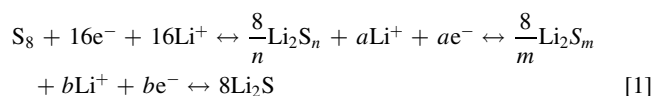
where $a = \frac{16(n-1)}{n}$, and $b = \frac{16(m-1)}{m}$.

One of the major hindrances to develop a high-performance Li-S battery is the uncontrolled dissolution of elemental sulfur (S_8)

and polysulfides, which leads to 1) the loss of active material and, 2) poor cycling efficiency caused by the so-called polysulfide shuttling.[1,3,6,7,9,10,13–15] Despite the great progress that has been made in cathode material development to contain the soluble species within the sulfur cathode electrode, the practical performance of current Li-S batteries is still far from satisfying. To further improve and optimize Li-S battery performance, the fundamental processes during charge and discharge need to be better understood, particularly with regards to the dominant polysulfide species in the different charge/discharge regimes.

To address this particular issue, many analytical techniques have been applied.[1,6,7,9,13,15–19] In one of the most referenced studies in the literature, Barchasz et al.[9] have investigated the Li-S system in a TEGDME-based (tetraethylene glycol dimethyl ether) electrolyte using *ex situ* liquid chromatography, UV–vis absorption spectroscopy, and electron spin resonance spectroscopy. In their study, S_6^{2-}/$S_3^{\cdot-}$ species are proposed to be formed at the 1st discharge plateau, which subsequently get reduced to S_4^{2-} in the transition region to the 2nd plateau, at which S_4^{2-} in turn is reduced to S_3^{2-}/S_2^{2-}/S_1^{2-} (note that S_1^{2-} here corresponds to the final Li_2S product).[9] Although much insights have been gained by this study, these *ex situ* results do not necessarily represent the real-time cell chemistry in an operating Li-S battery. Furthermore, this study does not provide insights into the cell chemistry in state-of-the-art electrolytes, i.e., with solvent mixtures of 1,3-dioxolane (DOL) and 1,2-dimethoxyethane (DME), as the stability of polysulfide (or radical) intermediates is largely influenced by the electrolyte solvents[6,7,9,10,17,20–24] (e.g., $S_3^{\cdot-}$ is better stabilized in TEGDME than in DME[10,25]). Moreover, the chemical equilibria in which polysulfides are involved, i.e., chain-breaking (e.g., $S_6^{2-} \leftrightarrow 2S_3^{\cdot-}$)[26] and disproportionation reactions (e.g., $S_8^{2-} \leftrightarrow S_6^{2-} + ¼S_8$),[6,7,9,10,13,21,26] can be easily shifted by the environmental change imposed by *ex situ* analysis (i.e., by either removing the electrolyte or by changing the solvent, the type and concentration of the conducting salt, and/or the temperature).[6,17,27,28]

Hence, various *operando* techniques have recently been developed to investigate the Li-S battery system,[1,7,8,12,13,18,29–32] e.g., *operando* X-ray diffraction (XRD)[31,32] and X-ray absorption near-edge spectroscopy (XANES).[7,8,18] Especially when using spatially
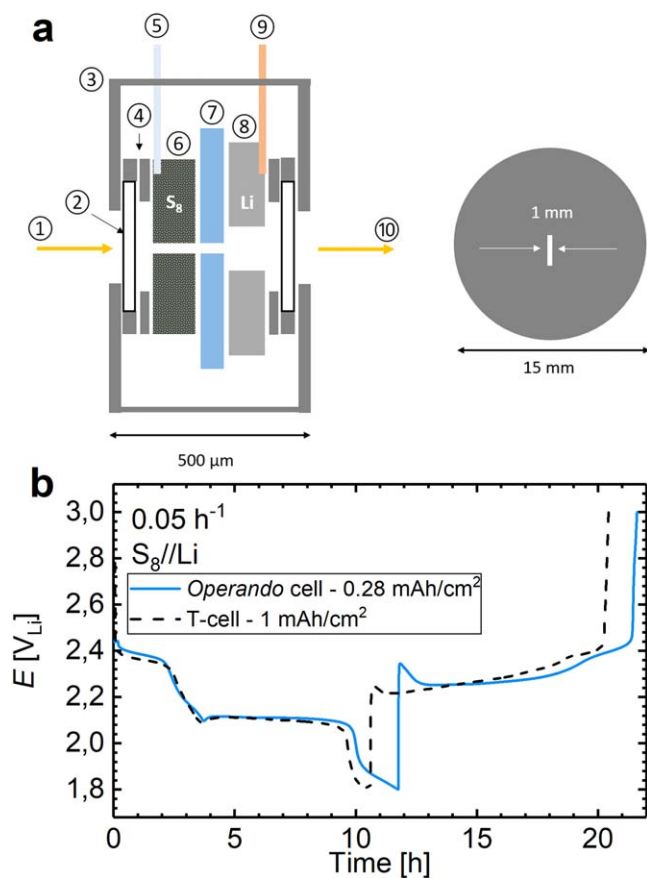
*Electrochemical Society Student Member.
**Electrochemical Society Fellow.
[a]Present Address: Business unit Battery Cell, Volkswagen Group Components, Salzgitter, Germany.
[b]Present Address: Hollingsworth and Vose Advanced Materials, Mysore-571311, India.
[z]E-mail: qi.he@tum.de

Figure 1. (a) Design and components of the UV–vis spectro-electrochemical cell (transmission mode). Left panel: (1) incident UV–vis beam, (2) quartz-glass ($\sim$165 μm thickness), (3) pouch foil (115 μm thickness), (4) pouch foil based sealing ring, (5) Al current collector tab ($\sim$100 μm thickness), (6) S_8/C composite based cathode coated onto an 18 μm thick Al foil ($\sim$60 μm total thickness), (7) separator (4 layers of Celgard H2013 with a total thickness of 80 μm), (8) anode electrode of either metallic lithium ($\sim$70 μm thickness) or pre-lithiated graphite coated onto an 11 μm thick Cu foil (total thickness of 60 μm), (9) Ni current collector tab ($\sim$100 μm thickness), (10) path of the transmitted beam. Right panel: top view of the cathode electrode with a slit (1 mm $\times$ 5 mm). (b) Galvanostatic cycling at a C-rate of 0.05 h^{-1} of the *operando* UV–vis spectroelectrochemical cell (blue line) with an S_8/C composite cathode (0.28 mAh cm^{-2}, with a slit), an Li-anode, and 200 μl electrolyte, benchmarked against a Swagelok® type T-cell (dashed line) with an S_8/C cathode (1 mAh cm^{-2}, without slit), an Li-anode, and 40 μl electrolyte. Electrolyte: DOL:DME (1:1, v:v) with 1 M LiTFSI and 0.5 M LiNO$_3$.

resolved *operando* XANES, both amorphous and crystalline S_8 and Li_2S as well as dissolved polysulfides (S_x^{2-}) and $S_3^{\cdot-}$ can be monitored during cell cycling in both the cathode electrode and in the separator.[7,8] This approach facilitated our comprehension of the evolution of species during the charge and discharge of an operating Li-S battery cell. Nevertheless, the exact reaction pathway of S_8 to Li_2S (or vice versa) still remains unclear, due to the large self-absorption effect in X-ray absorption spectroscopy, which allows neither differentiation of the various polysulfides nor a spectral deconvolution of the S_8 and polysulfide signals. The most practical technique to differentiate between various polysulfides is UV–vis spectroscopy that has been widely employed.[9,10,17,21,24,33–36] For instance, Patel et al.[24] have developed an *operando* UV–vis spectroscopy approach in reflectance mode, by which they were able to confirm that long-chain polysulfides are first formed after the initial S_8 reduction during discharge and that short-chain polysulfides are generated in the subsequent discharge process. However, the absorption shift in reflectance UV–vis spectra is difficult to interpret,

since it is greatly influenced by both the type of polysulfide species and their concentration. Hence, the identification of polysulfides in an operating Li-S battery using *reflectance* UV–vis spectroscopy is rather challenging.

On the other hand, the absorption shift in *transmission* UV–vis spectroscopy is only dependent on the chromophoric species themselves (i.e., on the specific polysulfide species), where the concentration of a given chromophore influences nothing but the absorption intensity. Therefore, *operando* UV–vis spectroscopy in transmission mode has been developed over the last two decades, mostly to investigate the cyclic voltammetric response of the various S-redox reactions in different electrolytes.[10,34,37–39] For example, it was observed that S_8^{2-} and $S_3^{\cdot-}$ are predominant in high donor number (high-DN) solvents such as dimethyl sulfoxid (DMSO) and N,N-dimethylformamide (DMF),[21,23,34,36,37,40] whereas S_4^{2-} is one of the most abundant species in low donor number (low-DN) solvents, for example in DOL:DME (1:1, v:v).[10,25] Unfortunately, the classic three-electrode cell design as well as the platinum or gold electrode used in these studies are inappropriate to investigate the conventional galvanostatic cycling of Li-S batteries. Specifically, the typical Li-S galvanostatic voltage profile is difficult to achieve in this open system, owing to the large diffusion distances of soluble S-species in such cells, which result in charge/discharge characteristics very different from conventional thin-layer configurations (e.g., pouch or coin cells). Thus, the inspection of the evolution of the intermediates during galvanostatic cycling of a Li-S cell with a conventional S_8/C composite cathode material is required to attain a deeper knowledge of Li-S reaction mechanism in an actual Li-S battery.

In this study, we present an *operando* transmission UV–vis cell design, benchmark its electrochemical performance, and apply it to identify the soluble reaction intermediates during the discharge of a Li-S battery with an S_8/C composite based cathode. In order to properly evaluate the obtained *operando* UV–vis spectra, we systematically analyze the reference spectra of different polysulfide solutions with a nominal stoichiometry ranging from "Li_2S_2" to "Li_2S_{16}" in DOL:DME-based electrolyte, based on which we propose a peak assignment for the various polysulfides. Thereupon, we obtain real-time *operando* UV–vis spectra during the discharge of a Li-S battery and propose for the first time a meta-stable polysulfide species (S_3^{2-}) that is present at substantial concentrations during the 2nd discharge plateau. We confirm the formation of this meta-stable S_3^{2-} in DOL:DME-based electrolyte by determining the number of electrons transferred for the reduction of "Li_2S_4" using the rotating ring disk electrode (RRDE) technique. To further investigate the electrochemical and chemical behavior of polysulfides of interest (S_4^{2-}, S_3^{2-}), we modify the galvanostatic cycling procedure by introducing constant voltage (CV) and open circuit voltage (OCV) phases during the operation of the *operando* UV–vis cell. Finally, we propose a discharge mechanism for Li-S batteries in DOL:DME-based electrolyte that incorporates both the findings from our *operando* UV–vis results and those from other *operando* studies in the literature, such as XANES[7,13] and XRD.[31]

Experimental

Operando *UV–vis cell design*.—The *operando* cell design is presented in Fig. 1a. It is a pouch cell based design, where two quartz glass windows ($\sim$165 μm thickness, with internal transmittance from 180 nm to 2000 nm greater than 0.99) are sealed into the front and back pouch foil (consisting of a multilayer of Nylon, aluminum and polypropylene), so that the UV–vis incident beam can pass through the *operando* cell onto the detector. The transmission of the incident beam is accomplished through a slit (1.0 mm $\times$ 5.0 mm) in both working electrode and separator as well as through a larger slit (2.5 mm $\times$ 8.0 mm) in the counter electrode to facilitate alignment, so that the soluble intermediates (S_n^{2-} and S_8) can freely diffuse into the slit and thus absorb UV–vis light of their characteristic wavelength. The slit size of 1.0 mm $\times$ 5.0 mm in the

working electrode is chosen to be large enough to enable a sufficiently large UV–vis beam to pass through the sample and small enough to reduce the time required for reaction intermediates to diffuse from the slit edge to the slit center. The estimated diffusion time is about 10 min, assuming the diffusivity of dissolved polysulfides to be $\sim 2.6 \cdot 10^{-6}$ cm^2 s^{-1} in DOL:DME-based electrolyte.[6] This estimation is confirmed by the *operando* data showing that dissolved chromophores can be detected already after at the 1st spectra ($\sim$12 min) taken during the charge of an Li$_2$S-Li cell (data not shown in this study).

Electrode preparation and electrochemical measurements.— *Cathode preparation.—*The preparation of the S$_8$/C composite (with 66.7wt% S$_8$ and 33.3wt% vulcan carbon (XC-72, Tanaka Kikinzoku Kogyo)) is described elsewhere in a detailed manner.[17,41] The as-prepared S$_8$/C composite was added to a dispersion of polyvinylidene difluoride (PVDF, HSV900, Kynar) in N-methyl-pyrrolidinone (NMP, 99.5%, anhydrous, Sigma-Aldrich), and the resulting suspension/ink was mixed in a plenary mixer (Thinky, Japan). It was then coated onto an 18 μm thick aluminum foil (MTI, USA) using a Mayer rod with different gaps to achieve the desired loading (from $\sim$0.15 mg$_s$ cm^{-2} ($\sim$0.25 mAh cm^{-2}) to $\sim$0.6 mg$_s$ cm^{-2} ($\sim$1.0 mAh cm^{-2})). The final cathode composition is 60wt% S$_8$, 30wt% vulcan carbon and 10wt% PVDF. The coating was initially dried at room temperature overnight, then electrodes were punched out as disks with a diameter of either 11 mm (for Swagelok®-type T-cells) or 15 mm (for coin cells and for *operando* UV–vis cells, whereby the punching tool for latter also cut out the above specified slit), and finally dried for another 12 h under static vacuum at 60 °C in a sealed glass oven (Büchi, Switzerland).

*Graphite anode preparation.—*Graphite (SLP30, Timcal, Japan) was mixed with PVDF in NMP to achieve an ink solids composition of 90wt% graphite and 10wt% PVDF. The resulting ink was mixed in a planetary mixer for 20 min and coated onto an 11 μm thick copper foil (99.99%, MTI, USA) using a Mayer rod with different gaps to achieve the desired loadings ranging from 1.3–2.2 mg$_{C6}$ cm^{-2} ($\sim$0.45 to $\sim$0.8 mAh cm^{-2}). The coating was initially dried at 50 °C overnight, then electrodes were punched out as disks with a diameter of 14 mm (for coin cells and for *operando* UV–vis cells, whereby the latter were also cut to contain the above specified slit), and finally dried for another 12 h under dynamic vacuum at 120 °C in a glass oven (Büchi, Switzerland). A smaller anode diameter (14 mm) and larger separator diameter (18 mm, Celgard H2013) were chosen to avoid short circuit during the slit alignment while assembling the *operando* cell; since all experiments with graphite anodes were conducted with pre-lithiated graphite electrodes and since only the first discharge of the sulfur working electrode was considered, artefacts from lithium plating which would be expected to occur on an undersized anode must not be considered.

The pre-lithiation of graphite electrodes was accomplished in a C$_6$//Li coin cell with an electrolyte consisting of 1 M lithium perchlorate (LiClO$_4$, battery grade, 99.99% trace metal basis, Sigma-Aldrich), 0.1 M LiNO$_3$ and 0.5 M vinylene carbonate (BASF SE, Germany) in DOL:DME (1:1, v:v). One formation cycle at 0.1 C followed by a galvanostatic lithiation to 50% SOC were performed in a climate chamber (Binder, Germany) at 25 °C. Afterwards, the preformed and partially pre-lithiated graphite electrodes were harvested and washed three times with DOL:DME (1:1, v:v) solution. The areal delithiation capacity of these pre-lithiated graphite electrodes consequently ranges from $\sim$0.2 to $\sim$0.4 mAh cm^{-2}.
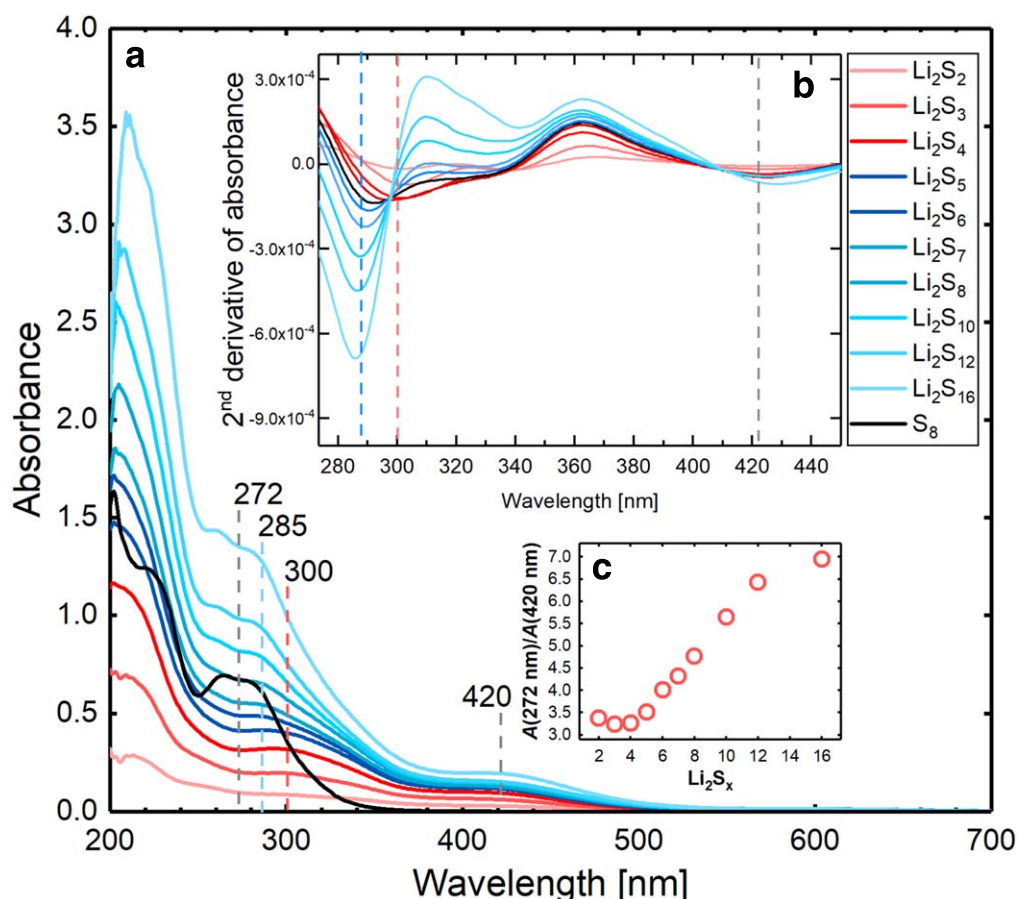
Figure 2. (a) UV–vis spectra of 1 mM "Li$_2$S$_x$" and 1 mM S$_8$ in DOL:DME (1:1, v:v) with 1 M LiTFSI, measured in an air-tight 1 mm thick cuvette at room temperature (25 $\pm$ 1 °C). (b) The inset shows the 2nd derivative of the obtained UV–vis spectra. (c) Ratio between the absorption at 272 nm (expressed as A (272 nm)) and at 420 nm (expressed as A(420 nm)) extracted from the spectra for all polysulfide samples.

Cell assembly and electrochemical measurements.—Electrochemical measurements were performed using Swagelok®-type T-cells, coin-cells (CR2031, Hohsen, Japan), and *operando* UV–vis pouch cells (see Fig. 1a). S_8/C composite cathodes were either paired with a lithium metal anode (99.9% purity with 70 or 450 μm thickness, Rockwood lithium, USA) or a pre-lithiated graphite electrode (~60 μm thickness). All cells were assembled in an Ar-filled glove box (<0.1 ppm O_2 and H_2O, Mbraun, Germany) and were connected either to a multi-channel potentiostat (VMP3, BioLogic, France) in a climate chamber (Binder, Germany) at 25 °C (±0.5 °C) or to a single-channel potentiostat (SP-200, BioLogic, France) in an air-conditioned room (25 ± 1 °C). Four layers of Celgard H2013 were used as separator, and the electrolyte used in this study consisted of a 1:1 (v:v) mixture of 1,3-dioxolane (DOL, anhydrous, 99.8%, Sigma-Aldrich) and 1,2-dimethoxyethane (DME, anhydrous, 99.8%, Sigma-Aldrich) with 1 M lithium bis(trifluoromethane) sulfonamide (LiTFSI, 99.95% trace metal basis, Sigma Aldrich; dried under dynamic vacuum at 120 °C for 3 d in a sealed glass oven) and 0.5 M (for benchmarking) or 0.1 M (for *operando* experiments) lithium nitrate (LiNO$_3$, 99.99% trace metal basis, Sigma-Aldrich; dried under dynamic vacuum at 110 °C for 3 d in a glass oven).

For the T-cells, 40 μl of electrolyte were used, while an excess of electrolyte (200 μl) is required for the *operando* UV–vis cell in order to wet the electrode separator assembly in such a way that the slits in the electrodes and the separator are filled completely with electrolyte, so that reaction intermediates can freely diffuse into the detection region (slit). Another limitation of the *operando* UV–vis Li-S battery cell is that it can only be operated with low-loaded S_8/C composite electrodes (~0.15 mg$_S$ cm^{-2}, corresponding to ~0.25 mAh cm^{-2}), as dissolved S_8 and polysulfides have rather high molar absorptivity (e.g., the molar absorptivity of S_8 at ~270 nm in DOL:DME (1:1, v:v) is ~7000 L·mol^{-1}·cm^{-1}, see black line in Fig. 2a), so that a maximum concentration of ~10 mM S_8 (dissolved) or ~20 mM S_4^{2-} can be resolved in our *operando* UV–vis cell (estimated with an effective path length of ~0.5 mm, an absorbance of 4 as the detection limit and without considering any co-existence of different polysulfides and/or S_8).

Acquisition of reference UV–vis spectra and **operando** *UV–vis spectra.*—We prepared polysulfides with nominal compositions corresponding to 1 mM "Li$_2$S$_x$" ($2 \leqslant x \leqslant 16$) by stoichiometrically mixing elemental sulfur (99.998%, trace metal basis, Sigma-Aldrich) and Li$_2$S (99.98% trace metal basis, Sigma-Aldrich),[42] and analyzed their absorption behavior systematically after stirring the solution for at least 12 h in an Ar-filled Glovebox (<0.1 ppm O_2 and H_2O, Mbraun, Germany). These reference spectra were taken using an air-tight cuvette with a 1 mm path length (1/ST/C/Q/1, Starna Scientific GmbH) at 25 °C (±1 °C).

The *ex situ* and the *operando* UV–vis measurements were carried out employing a Lambda 35 UV–vis spectrometer (Perkin Elmer, USA), which was switched on at least 30 min prior to any measurements. A scan rate of 60 nm min^{-1} was chosen to increase the signal/noise ratio, and therefore ~8 min were needed to scan the wavelength region from 230 nm to 700 nm with a step-size of 4 nm. Spectra were recorded every 12 min according to the estimated diffusion time of polysulfides into the probing slit (~10 min, see above). We thus carried out the galvanostatic cycling with a C-rate of 0.05 h^{-1} (referenced to a theoretical discharge capacity of 1675 mAh g$_S^{-1}$) to collect UV–vis spectra with a sufficiently high capacity resolution throughout the discharge process (ca. Δ17 mAh g$_S^{-1}$ per spectrum), so that for a typically 9 h long discharge roughly 45 UV–vis spectra can be recorded.

RRDE measurement.—The setup for RRDE measurements in non-aqueous electrolytes was adopted from that reported by Lu et al.[6] and Herranz et al.[43] It is a classic three-electrode cell, employing a working electrode consisting of a PTFE embedded glassy carbon disk working electrode with a diameter of 5.0 mm, and a gold ring

electrode with an internal diameter of 6.5 mm and an external diameter of 7.5 mm (Pine Research Instrumentation, USA). The working electrode compartment was filled with 4 mM nominally prepared "Li$_2$S$_4$" in DOL:DME (1:1, v:v) with 1 M LiTFSI. A Pt wire was employed as counter electrode in a separated compartment filled with same electrolyte and connected with the working electrode compartment by a glass frit. Ag/AgNO$_3$ (0.1 M) in acetonitrile (ACN) was used as reference electrode, which was separated with a Vycor frit from the working electrode compartment. The RRDE cell was flushed with Ar for 30 min prior to the measurement and blanketed with an Ar flow during the experiment. AC impedance measurements were taken by applying a voltage perturbation of 10 mV (1 MHz to 100 mHz) before the RRDE measurements, and the ohmic drop between reference electrode and working electrode was thereby determined to be ~80 Ω and was used to determine the iR-free voltage. The potentials measured by the Ag$^+$/Ag reference electrode was finally converted to the ferrocenium/ferrocene (Fc$^+$/Fc) reference potential scale (0 V vs Ag$^+$/Ag $\equiv$ +0.043 V vs Fc$^+$/Fc), as reported previously.[6,17]

Results and Discussion

Electrochemical benchmarking of the **operando** *UV–vis cell.*—The electrochemical performance of our *operando* UV–vis cell were first benchmarked against a Swagelok®-type T-cell with a standard electrolyte (1 M LiTFSI and 0.5 M LiNO$_3$ dissolved in DOL:DME (1:1, v:v)), using an S_8/C composite as working electrode, metallic lithium as counter electrode, and 4 layers of the H2013 separator. The cell voltage vs time for the first discharge and the first charge at a C-rate of 0.05 h^{-1} between 1.8 and 3.0 V$_{Li}$ is shown in Fig. 1b. The T-cell with a sulfur loading of 0.6 mg$_S$ cm^{-2} (corresponding to a theoretical capacity of 1 mAh cm^{-2}) and with a ratio of electrolyte volume to sulfur mass (E/S) of ~71 μl mg$_S^{-1}$ (black dashed line) reaches approximately 50% of its theoretical capacity and closely resembles that reported in the literature.[7,11,44–46] Here it should be noted, that an additional decreasing slope below 1.9 V is observed for the *operando* UV–vis cell, but not for Swagelok®-type T-cell. This phenomenon can be rationalized by the continuous electrochemical reduction of LiNO$_3$ below 1.9 V,[47] especially in the case of cycling at a small discharge current.

While for the above outlined reasons the sulfur loading of the *operando* UV–vis cell is much lower (0.17 mg$_S$ cm^{-2}, corresponding to a theoretical capacity of 0.28 mAh cm^{-2}) and while the E/S ratio is much larger (~700 μl mg$_S^{-1}$), its first discharge with two-plateaus around 2.35 V and 2.1 V separated with a super-saturation point (blue line) is quite comparable with the voltage profiles of Li-S cells with a practical E/S ratio of 8 μl mg$_S^{-1}$ that were reported by Hagen et al.[48] Therefore, we believe that the reaction pathway deduced from our *operando* UV–vis analysis, namely the reduction of S_8 to Li$_2$S$_2$/Li$_2$S is likely to also be operative in actual Li-S batteries despite their substantially lower E/S ratio.

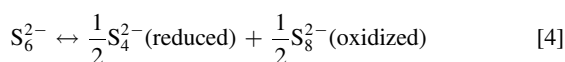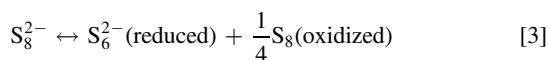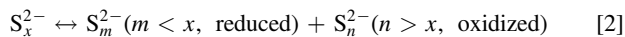*UV–vis Peak assignment for polysulfides in DOL:DME-based electrolyte.*—While the UV–vis peak assignment of various polysulfides have already been proposed in different electrolytes, such as in DME,[49] TEGDME,[9,33] DMSO,[21,35,36] DMF,[40,50] DMA,[23] ionic liquid,[51] a comprehensive peak assignment of polysulfides in DOL:DME-based electrolyte is, to the best of our knowledge, not available in the literature. Although the polysulfide speciation is similar in the solvents with comparable donor number,[17] their UV–vis peak position, intensity and the shape of the absorption spectra may still vary in those solvents, owing to the solvatochromism phenomenon.[52] In other words, the surrounding medium of a chromophore (e.g., solvent) may alternate the solvation of the ground and first-excited state of the chromophore,[52] which would result in a hypsochromic or bathochromic shift. Therefore, in order to unambiguously identify the reaction intermediates in a Li-S cell operating in the DOL:DME-based electrolyte, a comprehensive peak

assignment of polysulfides, specifically in the same DOL:DME-based electrolyte, is required.

The UV–vis spectra of 1 mM polysulfide samples of the nominal composition "Li_2S_x" ($2 \leqslant x \leqslant 16$) in DOL:DME (1:1, v:v) with 1 M LiTFSI are presented in Fig. 2a. The UV–vis spectra of the same polysulfide compositions in the same electrolyte with additional 0.1 M LiNO$_3$ are shown in Fig. S1 (available online at stacks.iop.org/JES/167/080508/mmedia) in order to confirm that the presence of 0.1 M LiNO$_3$ has no significant influence on the polysulfide composition (discussed in supplementary information section 2.1) and that it only adds a spectral feature at ~285 nm with a very small absorbance. All prepared polysulfides "Li_2S_x" ($2 \leqslant x \leqslant 16$) have three absorption regions, viz., around 400 nm, 300 nm, and 200 nm. We focus the peak assignment mainly on the regions of 400 nm and 300 nm, since the deconvolution of the UV–vis spectra below 250 nm is not possible in the presence of LiNO$_3$ (owing to its high absorbance in this region, see. Fig. S1), that will be required as additive for stable cycling in the *operando* UV–vis experiments.
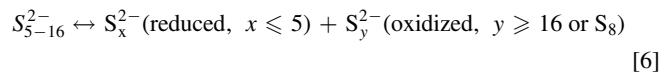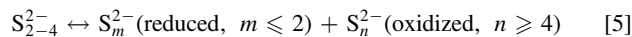
Spectral features of long and short-chain polysulfides.—Two groups of polysulfides are observed in Fig. 2, viz., short-chain polysulfides ("Li_2S_2"–"Li_2S_4," red lines) and long-chain polysulfides ("Li_2S_5"–"Li_2S_{16}," blue lines). Although both short-chain and long-chain polysulfides have a common absorption shoulder at ~420 nm, their absorption behavior in the region around 300 nm is distinct from each other. Specifically, the long-chain polysulfides (e.g., "Li_2S_{16}," "Li_2S_{12}") show a clear shoulder at 285 nm, while short-chain polysulfides exhibit a shoulder at ~300 nm. This difference in absorption behavior around 300 nm is well resolved in the 2nd derivative of the absorption spectra (Fig. 2b), a commonly used rather sensitive method to analyze shoulders and overlapping absorption bands.[53] It is well established that the minima in the 2nd derivatives of the absorption spectra correspond to the appropriate absorption maxima in the absorption spectra.[53] In Fig. 2b, short-chain polysulfides ("Li_2S_2"–"Li_2S_4," red lines) clearly show a minimum around ~300 nm, while long-chain polysulfides ("Li_2S_5"–"Li_2S_{16}") exhibit no minimum at ~300 nm but at ~285 nm.

We also observe that polysulfides within the each of the two polysulfide sub-groups, represented by the nominal compositions "Li_2S_5"–"Li_2S_{16}" (blue lines) and "Li_2S_2"–"Li_2S_4" (red lines), absorb at the same wavelength with different intensities, albeit their different nominal compositions. Considering the hypothesis that not every "Li_2S_x" can be stabilized in DOL:DME solution, we suggest that polysulfides absorbing at the same wavelength (e.g., "Li_2S_5"–"Li_2S_{16}") go through disproportionation reactions and thereby generate the same species but in different concentrations. In order to keep the charge conserved, the polysulfides involved in disproportionation reactions would have to have different oxidation states (as shown in Eq. 2, with specific examples given by Eqs. 3 and 4). To note, elemental sulfur (S_8) is considered to be a reasonable disproportionation product as shown[6,7,9,10,13,21,26] in Eq. 3.[9,54]

$$S_x^{2-} \leftrightarrow S_m^{2-}(m < x, \ reduced) + S_n^{2-}(n > x, \ oxidized) \quad [2]$$

$$S_8^{2-} \leftrightarrow S_6^{2-}(reduced) + \frac{1}{4}S_8(oxidized) \quad [3]$$

$$S_6^{2-} \leftrightarrow \frac{1}{2}S_4^{2-}(reduced) + \frac{1}{2}S_8^{2-}(oxidized) \quad [4]$$

In summary, we hypothesize that short-chain polysulfides and long-chain polysulfides go through disproportionation reactions to generate a few short-chain and long-chain polysulfides or dissolved sulfur which are most stable in the electrolyte. As for now, the specific composition of the polysulfide(s) formed by these disproportionation reactions cannot be specified, so that Eqs. 5 and 6 as well as the below listed Eqs. 7–10 are written as simplified

non-stoichiometric reactions.

$$S_{2-4}^{2-} \leftrightarrow S_m^{2-}(reduced, \ m \leqslant 2) + S_n^{2-}(oxidized, \ n \geqslant 4) \quad [5]$$

$$S_{5-16}^{2-} \leftrightarrow S_x^{2-}(reduced, \ x \leqslant 5) + S_y^{2-}(oxidized, \ y \geqslant 16 \ or \ S_8) \quad [6]$$

In preparing the "Li_2S_2" and "Li_2S_3" solutions, we noticed the presence of a white precipitate after 3 d heating (50 °C) and stirring, suggesting the formation of a thermodynamically stable insoluble sulfur-containing species. On the other hand, the "Li_2S_4" solution (as well as solutions with a nominally higher "polysulfide" composition) shows little/no precipitate. Even though Li_2S_2 is hypothesized to be solid,[55,56] it has never been experimentally isolated from a Li-S cell. We thus believe that the here observed white precipitate in "Li_2S_2" and "Li_2S_3" solutions is more likely Li_2S rather than Li_2S_2, whereby Li_2S is known to be insoluble in the DOL:DME-based electrolyte.[31,57] Thus, Li_2S (represented as S_1^{2-}) is a very likely candidate for the reduced S-species (S_m^{2-}) in Eq. 5, which can be re-written as:

$$S_{2-4}^{2-} \leftrightarrow S_1^{2-} + S_n^{2-}(oxidized, \ n \geqslant 4) \quad [7]$$
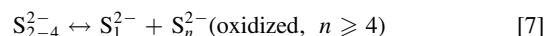
In addition, we note from Fig. 2 that long-chain polysulfides such as "Li_2S_{16}" and "Li_2S_{12}" show a clear absorbance in the 260–285 nm region as well as a clear shoulder at 285 nm, which resembles the characteristics of dissolved elemental S_8 that is marked in black in Fig. 2. Hence, we believe that dissolved S_8 (thermodynamically stable at ambient conditions[57]) is likely present in long-chain polysulfides solutions and can be considered as the oxidized S-species in Eq. 6, which can be re-written as:

$$S_{5-16}^{2-} \leftrightarrow S_x^{2-}(reduced, \ x \leqslant 5) + S_8 \quad [8]$$
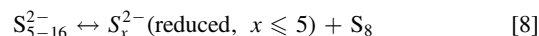
The analysis that suggests that S_{16}^{2-} or higher order polysulfides are not the oxidized species in Eq. 6 is discussed in the supplementary information (section 2.2 in the SI). Furthermore, it is clear that both short-chain polysulfides and long-chain polysulfides have a common absorption at ~420 nm, suggesting that all polysulfides may share a common species, viz., S_n^{2-}(Eq. 7) $\equiv S_x^2$ (Eq. 8). Consequently, Eqs. 7 and 8 can be re-written as:

$$S_{2-4}^{2-} \leftrightarrow S_1^{2-} + S_x^{2-} \quad [9]$$

$$S_{5-16}^{2-} \leftrightarrow S_8 + S_x^{2-} \quad [10]$$

Determination of the S_x^{2-} species.—Here we show that the ratio of the absorption at 272 nm (highest absorption characteristic of S_8) and 420 nm (assignment to S_x^{2-}), i.e., $\frac{A(272 \ nm)}{A(420 \ nm)}$ for all polysulfide samples are consistent with the predictions of Eqs. 9 and 10, and also provide a simple assessment of the common species (S_x^{2-}) that exists both in long-chain and short-chain polysulfide groups.

According to Eq. 9 (non-stoichiometric expression) or Eq. 11 (stoichiometric expression), the spectra of short-chain polysulfides would only have spectral characteristic features of S_x^{2-} (~420 nm and ~300 nm), as Li_2S (solid) would be UV–vis inactive in transmission mode. Therefore, the ratio $\frac{A(272 \ nm)}{A(420 \ nm)}$ would always be the same for short-chain polysulfides.

$$1Li_2S_m \leftrightarrow \frac{x - m}{x - 1}Li_2S(solid) + \frac{m - 1}{x - 1}Li_2S_x \quad [11]$$
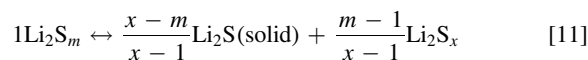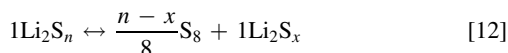
However, the ratio $\frac{A(272 \ nm)}{A(420 \ nm)}$ of long-chain polysulfides would increase linearly when the polysulfide chain length increases, since the disproportionation to S_8 would lead to a linear increase of A (272 nm) on account of the growing S_8 concentration, whereas the polysulfide concentration represented by A(420 nm) remains

Table I. Summary of the absorption characteristics assigned (in this work) to the chromophores dissolved in the DOL:DME-based electrolyte.

Chromophore	Absorption characteristics λ (nm)
S_8	$\sim$265–285
$LiNO_3$	$\sim$285
S_4^{2-}	300, 420
S_3^{2-}	$\sim$266

constant, as shown by the stoichiometric expression in Eq. 12.

$$1Li_2S_n \leftrightarrow \frac{n-x}{8}S_8 + 1Li_2S_x \qquad [12]$$

Since S_8 bears only a characteristic absorption at $\sim$272 nm but none at $\sim$420 nm (shown in black in Fig. 2a), the ratio $\frac{A(272\,nm)}{A(420\,nm)}$ of long-chain polysulfides based on Eq. 12 can be written as:

$$\frac{A(272\,\text{nm})}{A(420\,\text{nm})} = \frac{A(S_8@272\,\text{nm}) + A(Li_2S_x@272\,\text{nm})}{A(Li_2S_x@420\,\text{nm})}$$
$$= \frac{A(S_8@272\,\text{nm})}{A(Li_2S_x@420\,\text{nm})} + a \qquad [13]$$

where a is a constant that represents the fixed ratio of $\frac{A(Li_2S_x\,@\,272\,nm)}{A(Li_2S_x\,@\,420\,nm)}$. A correlation between the ratio $\frac{A(272\,nm)}{A(420\,nm)}$ and the nominal polysulfide chain length is shown in Fig. 2c, in which a horizontal line for short-chain polysulfides ("Li_2S_x," $x \leqslant 4$) and a line with a positive slope for long-chain polysulfides ("Li_2S_x," $x \geqslant 5$) are observed. In theory, the intersection of both lines should indicate the common species Li_2S_x, which could be "Li_2S_4" (likely) or "Li_2S_5" (still possible) in this case. Considering the S_4^{2-} assignment in DMSO (420 nm,[21] 435 nm[36]) and in TEGDME (420 nm[9]), we here also assign the spectral features at $\sim$420 nm and at $\sim$300 nm to S_4^{2-} in DOL:DME-based electrolyte. The absorption ratios of this two absorption characteristics of S_4^{2-} $\left(\frac{A(300\,nm)}{A(420\,nm)}\right)$ in nominally prepared "Li_2S_2" "Li_2S_3" "Li_2S_4" are presented in Fig. S2 (section 2.3 in the SI). A summary of the peak assignment for the chromophores dissolved in DOL:DME-based electrolyte is shown in the Table I.

Operando *identification of reaction intermediates in DOL: DME-based electrolyte.*—Here we employ our *operando* UV–vis cell to identify the reaction intermediates during the first discharge of Li-S batteries in DOL:DME-based electrolyte. We apply three different first discharge procedures to better understand the discharge process of Li-S batteries: 1) the conventionally used constant current (CC) discharge (referred to as "CC," as shown in Fig. 3a; 2) a CC discharge with constant voltage (CV) hold at the end of the 1st discharge plateau (CC-CV), followed by a constant current discharge to the end of the 2nd discharge plateau, and a final CV hold (referred to as "2(CC-CV)," shown in Fig. 4a; and, 3) a CC-CV discharge for the 1st plateau (as in 2), followed by a CC discharge into the onset of the 2nd discharge plateau, and a final open circuit voltage (OCV) phase (referred to as "CC-CV-CC-OCV," shown in Fig. 6a). As anode in these *operando* UV–vis cell experiments, we use pre-lithiated graphite rather than lithium metal, as the latter was shown to introduce changes in the spectroscopic background during cell cycling owing to the chemical reactions between lithium metal and electrolyte salt and/or solvent, which is further discussed in the section 3.1 of SI. Representative electrochemistry when employing pre-lithiated and pre-formed graphite instead of lithium metal in lithium-sulfur batteries has been shown in our previous study.[18] No background correction (subtraction of pure electrolyte in the *operando* cell configuration) is performed for the UV–vis analysis in order to prevent any overcorrection due to cell-to-cell variations in terms of slit alignment (on separator/electrodes) and beam

alignment. Thus, the obtained *operando* UV–vis spectra in this study are only adjusted to have the same baseline (at 700 nm).

Analysis of the polysulfide species formed during the 1st discharge plateau.—Figure 3a shows the voltage profile for a conventional constant current (CC) discharge in our *operando* UV–vis cell at a C-rate of 0.05 h^{-1}. Two well-defined discharge plateaus and a clear transition region between the 1st and the 2nd discharge plateau can be seen, and a reasonable discharge capacity ($\sim$45% of the theoretical capacity) is achieved, despite the high electrolyte volume to sulfur mass (E/S) ratio and the slit in the separator. Figures 3b–3d show the evolution of the *operando* UV–vis spectra during the first constant current discharge.

The very first UV–vis spectrum (lightest blue) in Fig. 3b is taken during the initial OCV phase prior to the first discharge ($\sim$30 min after cell assembly). An absorption at 265–285 nm in this spectrum is assigned to S_8, evident from the comparison with the reference spectrum obtained from the electrolyte with 1 mM S_8 (acquired in a cuvette; red line), and therefore indicating the dissolution of elemental S_8 from the S_8/C cathode upon exposure to the electrolyte. At the start of discharge, the S_8 features (265–285 nm) gradually weaken and two additional shoulders appear in the spectra, namely at $\sim$300 nm and at $\sim$420 nm, which have been attributed to S_4^{2-} in the peak assignment analysis of our *ex situ* data with reference solutions (Fig. 2). At the end of the first discharge plateau (at $\sim$1.4 h), the UV–vis spectrum is dominated by S_4^{2-} features, suggesting that by the end of the first discharge plateau, most S_8 has been reduced to S_4^{2-}, consistent with the hypothesis reported by Waluś et al.[31] using *operando* XRD. This might seem surprising, as the first step of S_8-reduction is generally considered to be the reduction of elemental S_8 to S_8^{2-}[6,21,34,36,37,39,58]:

$$S_8 + 2e^- \rightarrow S_8^{2-} \qquad [14]$$

However, no significant additional absorption features other than those of S_8 (265–285 nm) and S_4^{2-} ($\sim$300 nm, $\sim$420 nm) are visible in Fig. 3b, consistent with the observation reported by Zou and Lu[10] in DOL:DME (1:1, v:v) electrolyte with 1 M LiTFSI. This absence of additional absorption characteristics can be rationalized by the instability of S_8^{2-} in DOL:DME-based electrolyte, i.e., any S_8^{2-} intermediate either undergoes a fast subsequent electrochemical reduction (Eq. 15) or/and a chemical disproportionation (Eq. 16) before it can diffuse to the detection region (i.e., to the slit through which the UV–vis beam is passing), which is estimated to occur within $\sim$12 min. This fast conversion of S_8 to S_4^{2-} in DOL:DME (1:1, v:v) electrolyte with 1 M LiTFSI has also been reported in our previous work,[6] where we have shown a direct electron transfer process with >4 e$^-$/S_8 for S_8 reduction within the time scale of an RRDE experiment (seconds to[6,21,28,34,58] minutes).[9,54]

$$S_8^{2-} + 2e^- \rightarrow 2S_4^{2-}, \qquad [15]$$

$$S_8^{2-} \leftrightarrow \frac{1}{2}S_8 + S_4^{2-}, \qquad [16]$$
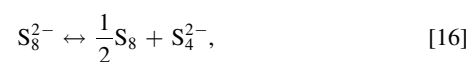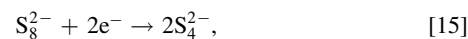
Based on the Beer–Lambert law, one can estimate the observed maximum S_4^{2-} concentration in the *operando* cell from its characteristic adsorption at 420 nm that, as shown in Fig. 3b, reaches a maximum of $\sim$1.1 absorbance units over a background of $\sim$0.44 absorbance units, i.e., a net absorbance of $\sim$0.66:

$$c(S_4^{2-}) = \frac{A_{net}(420\,\text{nm})}{b*\varepsilon(420\,\text{nm})}$$
$$= \frac{0.66}{0.04\,\text{cm}*1033\,\text{l}*\text{mol}^{-1}\text{cm}^{-1}}$$
$$\approx 16\,\text{mM} \qquad [17]$$

where $\varepsilon(420\,nm)$ is the molar absorptivity of S_4^{2-} at 420 nm, determined by *ex situ* samples, as shown in Fig. S4, and b is the
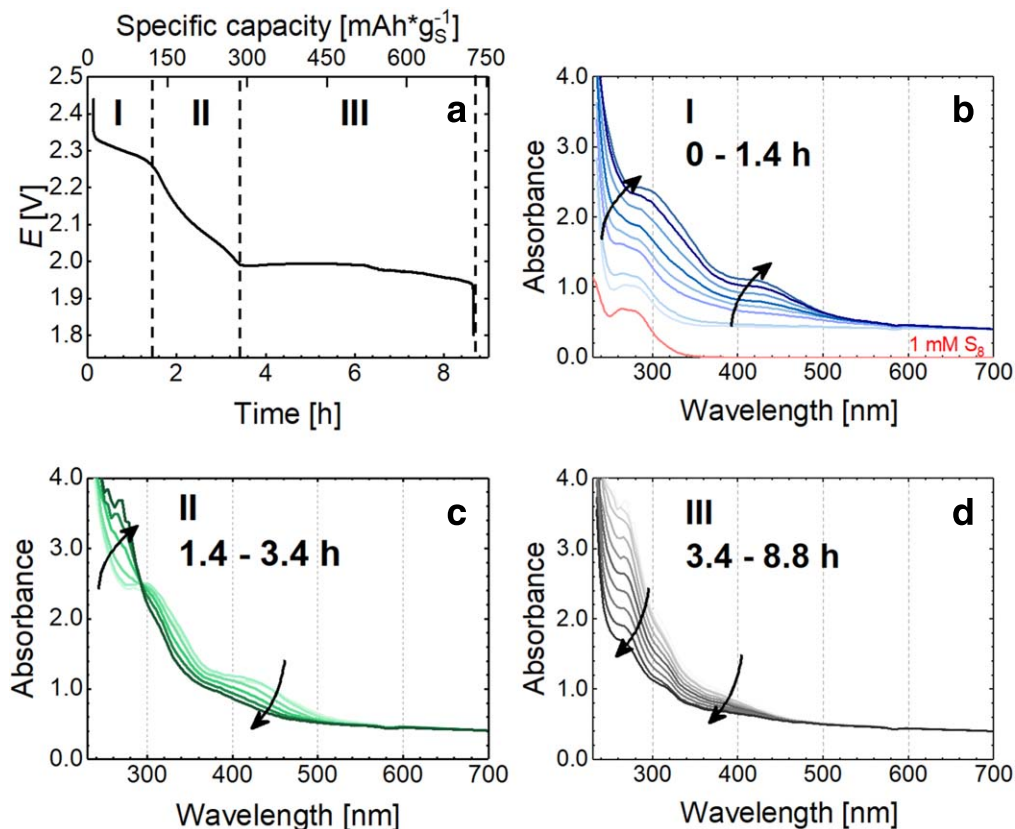
Figure 3. *Operando* UV–vis spectra for a conventional constant current (CC) discharge at a C-rate of 0.05 h^{-1} (referred to as "CC"). (a) Discharge voltage vs time of the *operando* UV–vis cell with an S$_8$/C cathode (0.17 mAh cm^{-2}), a graphite anode pre-lithiated to 50% SOC (referred to as LiC$_6$ (50% SOC), with ∼0.22 mAh cm^{-2} delithiation capacity), four separators (Celgard H2013), and 200 μl of DOL:DME (1:1, v:v) with 1 M LiTFSI and 0.1 M LiNO$_3$. The *operando* UV–vis spectra are shown for three different voltage regions (see panel (a)): (b) for the 1st discharge plateau (I), showing one spectrum every ∼0.2 h; (c) for the transition between the 1st and the 2nd discharge plateau (II), showing one spectrum every ∼0.4 h; and, (d) for the 2nd discharge plateau, showing one spectrum every ∼0.6 h.

beam path length through the *operando* UV–vis cell (∼0.04 cm). Alternatively, we can also estimate the maximum average S$_4^{2-}$ concentration in the cell specified in Fig. 3, based on the total amount of sulfur in the cell (0.17 mg) and the total amount of electrolyte (200 μl), resulting in ∼6.8 mM S$_4^{2-}$. This higher value calculated from the Beer–Lambert law can be explained by the necessarily inhomogeneous distribution of polysulfides over this rather short time scale (∼1.4 h), since a significant fraction of the electrolyte will be outside the active area (i.e., outside the 15 mm electrode diameter) so that homogenous mixing would be expected to be very long.

In the transition region between the 1st and 2nd plateau, the absorption at ∼420 nm and ∼300 nm drops quickly (Fig. 3c), while another so far unidentified absorption feature at ∼266 nm increases rapidly until the end of this transition region. This unidentified absorption feature becomes a dominate feature at the 2nd discharge plateau and decreases slowly until the end of discharge with a small residual signal remaining at the end of discharge (see Fig. 3d). Here is should be noted that the small shoulder at ∼326 nm in Fig. 3d originates from the lamp switch (from Vis-lamp to UV-lamp) of the UV–vis spectrometer.

Analysis of the S$_x^{2-}$ species formed after 1st discharge plateau.— To validate that the observed strong absorption at ∼266 nm that appears in the transition from the 1st to the 2nd discharge plateau is not an artefact and to achieve a higher time resolution, we modified the cycling procedure to include a constant voltage (CV) phase (labeled as region II in Fig. 4a) at the end of the 1st discharge plateau (labeled as region I in Fig. 4a), at a point just prior to the appearance of this feature at ∼266 nm. This was followed by another CC

discharge, for which we noted two spectroscopically distinct regimes, one until the onset of the 2nd discharge plateau (transition region between 1st and 2nd discharge plateau, region III) and one until the end of the 2nd discharge plateau (region IV). This was followed by another CV phase at the final potential of 1.85 V (region V) and the entire procedure will be referred to as "2(CC-CV)" discharge. Analagous to what was shown in Fig. 3b, elemental S$_8$ (∼265–285 nm) is reduced to S$_4^{2-}$ (∼300 and ∼420 nm) during the 1st discharge plateau (see Fig. 4b). Throughout the subsequent CV phase (at ∼2.2 V, see Fig. 4c) marked as region II, the absorption of S$_4^{2-}$ (at ∼300 and 420 nm) keeps increasing gradually, which confirms that S$_4^{2-}$ is stable at 2.2 V, contrary to S$_8$. The minor but still noticeable increase of the absorbances A(∼420 nm) and A(∼300 nm) of S$_4^{2-}$ in the CV phase in region II can be rationalized by the continuous reduction of residual S$_8$ that is dissolved in the electrolyte, in regions of the *operando* cell that are not in close proximity to the working electrode. The last two spectra in Fig. 4c are essentially identical, suggesting that the polysulfides formed in the *operando* cell are in equilibrium and that the S$_4^{2-}$ concentration has reached its maximum. Next, the *operando* cell is discharged further at constant current through the transition region between the 1st and the 2nd discharge plateau (region III in Fig. 4a). Consistent with the spectra shown in Fig. 3c (labeled there as region II), we also observe for the transition region in Fig. 4d that the absorption at ∼300 and ∼420 nm drops significantly while the absorption at ∼266 nm increases strongly over the ∼1.5 h duration of the transition region. Once the 2nd discharge plateau is reached (region IV in Fig. 4a), the absorption at ∼266 nm starts to decrease continuously (purple colored lines in Fig. 4e). This trend continues over the 3 h CV phase at ∼1.85 V (region V in Fig. 4a) that is
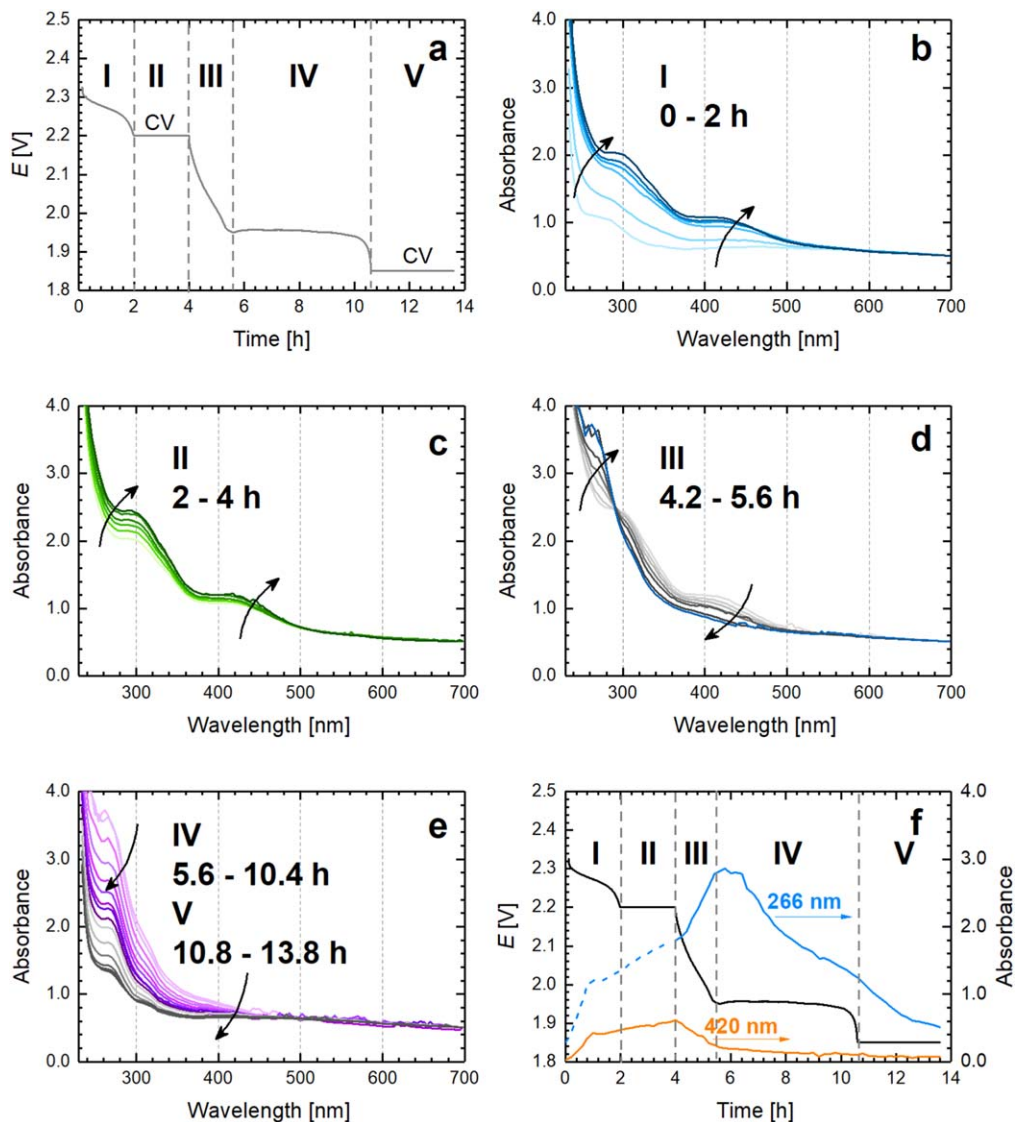
Figure 4. *Operando* UV–vis spectra for a CC discharge at 0.05 h^{-1} C-rate with a 2 h CV hold at the end of the 1st discharge plateau (regions I & II), followed by a CC discharge at 0.05 h^{-1} to the end of the 2nd discharge plateau (regions III & IV), and a final CV hold (region V) (referred to as "2(CC-CV)"). (a) Discharge voltage vs time of the *operando* UV–vis cell with an S$_8$/C cathode (0.24 mAh cm^{-2}), a graphite anode pre-lithiated to 50% SOC ($\sim$0.4 mAh cm^{-2} delithiation capacity), four separators (Celgard H2013), and 200 μl of DOL:DME (1:1, v:v) with 1 M LiTFSI and 0.1 M LiNO$_3$. The *operando* UV–vis spectra are shown for five different voltage regions: (b) for the 1st discharge plateau (I; one spectrum every $\sim$0.4 h); (c) for the CV hold at the end of the 1st discharge plateau (II; one spectrum every $\sim$0.4 h); (d) for the CC discharge during the transition from the 1st to the 2nd discharge plateau (III; one spectrum every $\sim$0.2 h); and, (e) for the CC discharge during the 2nd discharge plateau (IV; one spectrum every $\sim$0.6 h; purple lines), and for the final CV hold (V; one spectrum every $\sim$0.6 h; gray/black lines). (f) Evolution of the baseline corrected absorbance at 266 nm (blue) and 420 nm (yellow) in the *operando* cell along with the voltage profile (black). Since several chromophores strongly absorb at 266 nm (e.g., S$_8$, S$_4^{2-}$, and S$_x^{2-}$), we separated its evolution into two regions, viz., one before (dash blue line) and one after the S$_x^{2-}$ formation (solid blue line), which demonstrates that different processes contribute to the absorbance at 266 nm.

applied at the end of the second discharge plateau (see gray/black lines in Fig. 4e).

With the here described modified "2(CC-CV)" discharge procedure, we thus confirmed that the absorption at $\sim$266 nm is not an artefact but an actual absorption from an as yet unidentified chromophore in the *operando* UV–vis cell. Considering the possible chromophore (S$_8$, S$_x^{2-}$, electrolyte consisting of DOL:DME (1:1, v: v), LiTFSI, LiNO$_3$) and comparing the already established UV–vis spectra of S$_8$ (Fig. 3b, red line) and of the electrolyte (Fig. S3c in section 3.1 of the SI), we propose that these unidentified species with absorption $\sim$266 nm correspond to an as yet uncharacterized polysulfide species S$_x^{2-}$. In contrast to the here shown results, this absorption at $\sim$266 nm was not observed by Zou and Lu[10] in DOL: DME-based electrolyte, who exploited a spectroelectrochemical cell (cuvette-based design by employing a gold working electrode placed into a 1 mm thick cuvette) to investigate the cyclic voltammogram of

the sulfur electrode in a Li-S cell. After careful analysis, we believe that this discrepancy is related to differences in the potential and time resolution over the discharge process. While our "CC" and "2(CC-CV)" discharge procedures require $\sim$9 and $\sim$14 h, respectively, over the $\sim$500 mV discharge potential range (from 2.35 V to 1.85 V), during which spectra are taken every $\sim$10 min, the entire discharge process over a range of 700 mV (from 2.4 V to 1.7 V vs a lithium metal anode) is completed within $\sim$12 min in the study by Zou and Lu.[10] The unidirectional diffusion across the 1 mm thick cuvette in their case may not fulfill the thin-layer (diffusion) condition,[59] which might complicate the deconvolution of the overlapping spectra of unreacted S$_8$ and the various formed polysulfides, especially in the region below 300 nm.

Figure 4f shows the evolution of two of the major absorption features over the course of discharge, namely that at $\sim$266 nm and that at $\sim$420 nm. While the $\sim$420 nm feature is an exclusive

characteristic of S_4^{2-}, the absorption at ~266 nm is shared by S_8, S_4^{2-}, and the as yet unidentified S_x^{2-} species, so that a careful interpretation of the evolution of the absorption feature at ~266 nm is required. Clearly, the drastic increase of the absorption at ~266 nm in the transition region (region III in Fig. 4f) is accompanied by a strong decrease of the absorption at ~420 nm, suggesting a conversion of S_4^{2-} species (marked by the ~420 nm absorption) to species with a characteristic absorption at ~266 nm. Considering that this process only happens after the 1st discharge plateau, where dissolved S_8 is no longer present, and considering that the concentration of S_4^{2-} is clearly decreasing (orange line in Fig. 4f), we assign this increase of the adsorption at ~266 nm to the unidentified S_x^{2-} species, which must be a soluble reduction product of S_4^{2-}, i.e., either S_3^{2-} or S_2^{2-}.
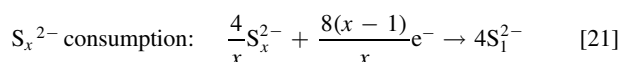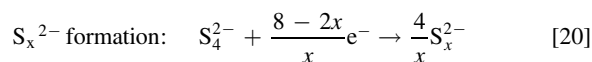
We also observe that the absorption at ~266 nm is the dominant absorption feature in the *operando* cell after the transition region between the 1st and the 2nd discharge plateau, which suggests that the conversion of these S_x^{2-} species to Li_2S must be the main process that occurs during the 2nd discharge plateau. In this case, the conversion of the S_x^{2-} species to Li_2S could in principle contribute ~50% ($x = 2$) or ~67% ($x = 3$) of the total theoretical capacity of a Li-S battery. Bearing in mind that the decrease in capacity with increasing C-rate is generally accompanied by a loss of capacity in the 2nd discharge plateau,[6,11] the conversion of the S_x^{2-} species to Li_2S is likely the rate limiting process in Li-S batteries. Therefore, it would be desirable to identify S_x^{2-} ($x = 3, 2$) and its possible reaction pathways during the 2nd discharge plateau in order to develop a better understanding of the Li-S chemistry in DOL:DME-based electrolytes.

S_3^{2-} was reported several times as a hypothetic species in Li-S chemistry, mostly as the reduction product of the S_3^{-} radical[10,20,23,34,35]:

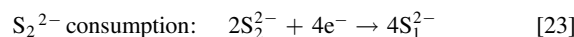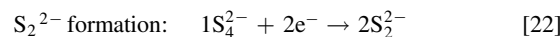$$S_3^{\bullet -} + e^- \rightarrow S_3^{2-} \qquad [18]$$

S_3^{2-} was proposed to be a soluble species in DMSO[10,34,35] and in DMA,[20,23] with an UV–vis absorption at ~270 nm in DMSO.[35] However, there are no experimental data that would prove the existence of S_3^{2-} in DOL:DME-based electrolyte (consisting of low donor number solvents) or even its possible UV–vis characteristics. Similarly, Li_2S_2 was suspected to be present as a solid in Li-S batteries, yet no actual experimental evidence was provided.[55] In the following, we will first assume that both Li_2S_2 and Li_2S_3 could be present as dissolved species in DOL:DME-based electrolyte and that they could be UV–vis active.

Identification of the S_x^{2-} species via comparison of transferred charges.—Based on the above discussion, the reduction pathway from S_4^{2-} present at the end of the 1st discharge plateau to Li_2S (here referred to as S_1^{2-}) present at the end of the 2nd discharge plateau (Eq. 19) would presumably go through an intermediate reduction step involving S_x^{2-}, as described generally in Eqs. 20 and 21 which sum up to Eq. 19:
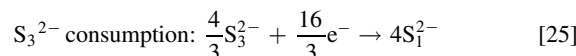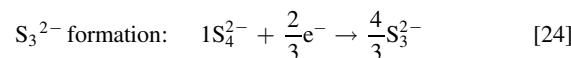
$$S_4^{2-} + 6e^- \rightarrow 4S_1^{2-} \qquad [19]$$

$$S_x^{2-} \text{ formation:} \quad S_4^{2-} + \frac{8 - 2x}{x}e^- \rightarrow \frac{4}{x}S_x^{2-} \qquad [20]$$

$$S_x^{2-} \text{ consumption:} \quad \frac{4}{x}S_x^{2-} + \frac{8(x - 1)}{x}e^- \rightarrow 4S_1^{2-} \qquad [21]$$

Evidence for an intermediate species in the transition region between 1st and 2nd discharge plateau, i.e., for the above suggested S_x^{2-} species can also be seen in the dQ/dV plot for the galvanostatic charge/discharge of an S_8/C//Li cell, with a discharge peak potential of ~2.2 V vs Li^+/Li, which corresponds to ~2.1 V vs the graphite anode pre-lithiated to 50% SOC (see Fig. S6 in section 3.4 of the SI). As discussed above, we believe that the S_x^{2-} species in Eqs. 19

and 20 are either S_2^{2-} or S_3^{2-}. In the case of S_2^{2-}, Eqs. 20 and 21 can be written as follows:

$$S_2^{2-} \text{ formation:} \quad 1S_4^{2-} + 2e^- \rightarrow 2S_2^{2-} \qquad [22]$$

$$S_2^{2-} \text{ consumption:} \quad 2S_2^{2-} + 4e^- \rightarrow 4S_1^{2-} \qquad [23]$$

On the other hand, if the S_x^{2-} species were to correspond to S_3^{2-}, Eqs. 20 and 21 would transform into:

$$S_3^{2-} \text{ formation:} \quad 1S_4^{2-} + \frac{2}{3}e^- \rightarrow \frac{4}{3}S_3^{2-} \qquad [24]$$

$$S_3^{2-} \text{ consumption:} \quad \frac{4}{3}S_3^{2-} + \frac{16}{3}e^- \rightarrow 4S_1^{2-} \qquad [25]$$

In the following, we present two different analysis approaches that suggest that the S_x^{2-} species do not correspond to S_2^{2-}, and instead indicates that they correspond to S_3^{2-}. We first compare the actually measured electrons/charges transferred in the experiment shown in Fig. 4a with that predicted by each set of the two intermediate reaction steps (Eqs. 22 and 23 for S_2^{2-} or Eqs. 24 and 25 for S_3^{2-}). Furthermore, we utilize the rotating ring disk electrode (RRDE) technique to directly determine the electrons transferred for the reduction step represented by $S_4^{2-} \rightarrow S_x^{2-}$. Both analysis approaches reveal consistent results and are presented in the following.

One way to differentiate the two reaction pathways is to compare the electrons transferred in the two intermediate reaction steps (Eqs. 22 and 23 for S_2^{2-} or Eqs. 24 and 25 for S_3^{2-}). For example, if the intermediate species were to be S_2^{2-}, Eq. 22 would imply that 2 S_2^{2-} would be generated from 1 S_4^{2-} with the transfer of 2 e^-. In this case, a maximum of another 4 e^- can be transferred to form 4 S_1^{2-} (based on Eq. 23, assuming 100% conversion). Therefore, the ratio of electrons transferred in the Eq. 23 (S_2^{2-} consumption) over that in the Eq. 22 (S_2^{2-} formation) would be $\frac{\# \text{ e in eq. } 23}{\# \text{ e in eq. } 22} \leqslant 2$, whereby a value of 2 would be expected for a 100% conversion of S_2^{2-} to S_1^{2-}. Similarly, if S_3^{2-} would be the intermediate, the ratio of electrons transferred in the Eq. 25 (S_3^{2-} consumption) over that in the Eq. 24 (S_3^{2-} formation) would be $\frac{\# \text{ e in eq. } 25}{\# \text{ e in eq. } 24} \leqslant 8$.

In the following, we will correlate this analysis of transferred electrons to the voltage profile shown in Fig. 4a, which is replotted in Fig. 5a (there, region V is omitted for clarity). More specifically, we will assign the region III and IV in the voltage profile (Fig. 5a) to the intermediate step of S_x^{2-} formation (Eqs. 20) and of S_x^{2-} consumption (Eqs. 21), respectively. In order to do so, this assignment requires that at the end of the first plateau and after the CV hold (i.e., at the end of region II in Fig. 4a) S_4^{2-} species are predominant and have reached their maximum concentration, corresponding to an essentially complete conversion of S_8 to S_4^{2-}. This is suggested by the last two spectra in Fig. 4c and also by the spectral analysis discussed in section 3.3 of the SI. It also requires that the generated S_4^{2-} is largely consumed during the transition region (region III), as is indeed suggested by the UV–vis data in Fig. 4f (see orange line based on the absorbance at 420 nm) and by the rather facile reduction of S_4^{2-} based on the rapid decrease of A (420 nm) in this region. Finally, for the here proposed sequential reactions (either Eqs. 22/23 or Eqs. 24/25), one would expect that the formed intermediate S_x^{2-} species would reach their maximum concentration at the end of the transition region, as indeed is indicated by the maximum absorbance at ~266 nm at the end of region III, albeit the consumption of S_4^{2-} and the absence of S_8 (see blue line in Fig. 4f). Based on these considerations, it is reasonable to assume that the process in region III follows Eqs. 22 or 24 (formation of S_x^{2-}) and that the process in region IV follows Eqs. 23 or 25 (consumption of S_x^{2-}), as was hypothesized above.

An evaluation of the charges transferred in the 2nd discharge plateau (region IV) and in the transition region (region III) from the
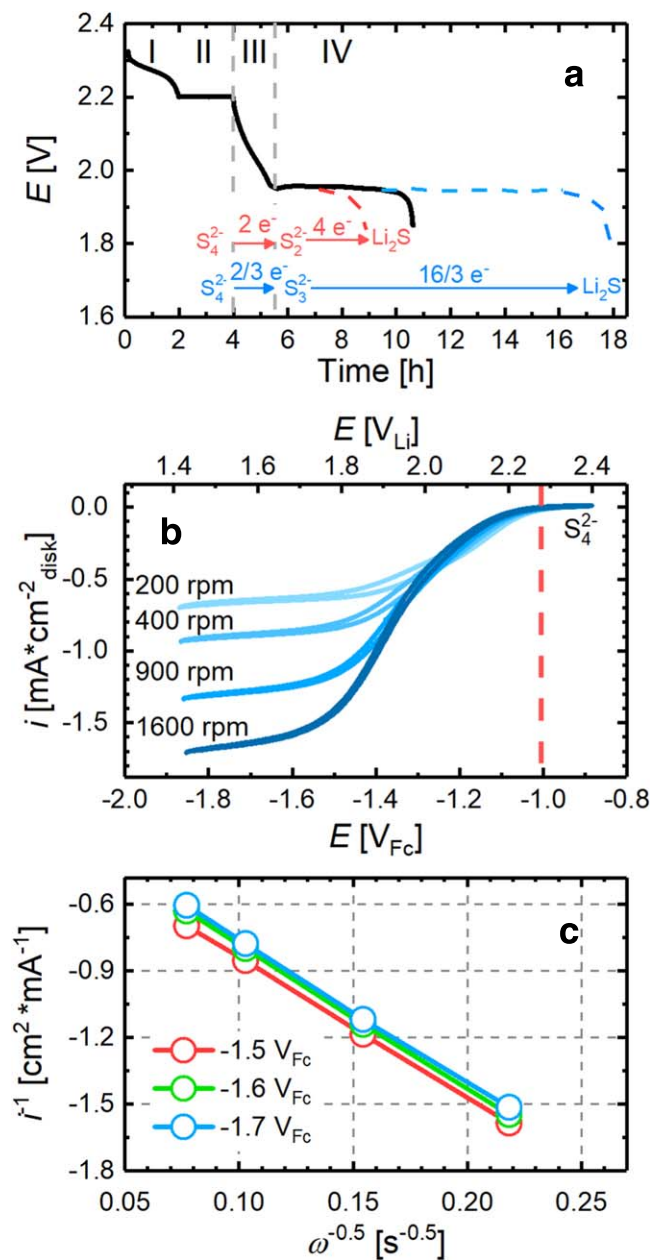
Figure 5. (a) Voltage profile of *operando* UV–vis cell replotted from Fig. 4 (the final CV phase is omitted here for clarity); the red printed reaction sequence corresponds to Eqs. 22 and 23 and the dashed red line sketches of the expected final discharge capacity for this reaction sequence, while the blue printed reaction sequence corresponds to Eqs. 24 and 25 and the dashed blue line sketches of the expected final discharge capacity for this reaction sequence. (b) Rotating ring disk electrode experiment: capacitively and ohmically corrected disk currents recorded vs the Li⁺/Li or the Fc⁺/Fc potential (note that that the Li⁺/Li potential is ∼0.1 V negative of the pre-lithiated graphite electrode) plotted at 50 mV s⁻¹ in Ar-saturated solution of 4 mM "Li₂S₄" with 1 M LiTFSI DOL:DME (1:1, v:v). (c) Koutecky-Levich plot of 1/i vs 1/ω⁻⁰·⁵ (with ω in rad s⁻¹) at different potentials.

operando UV–vis data in Fig. 4a (replotted in Fig. 5a) yields a charge ratio value of $\frac{Q(\text{region IV})}{Q(\text{region III})} = 3.3$, which is greater than the maximum value of $\leqslant 2$ that would be expected for an S_2^{2-} intermediate, but smaller than the value of $\leqslant 8$ that would be expected for an S_3^{2-} intermediate (also illustrated by the red and blue colored reaction sequences in Fig. 5a). Consistent with our results, it is often reported that in DOL:DME-based Li-S batteries the capacity delivered by the 2nd discharge plateau is at

least twice as large as the capacity delivered in the transition region.[1,6,7,11,13,15,18,27,47,48] In cells where the polysulfide redox shuttle is prevented by using an Li⁺ conducting glass ceramic (LiCGC) in which ∼100% discharge capacity was achieved at C/17, this ratio is as large as ∼5.[6] The fact that the here found charge ratio is larger than that of $\leqslant 2$ expected for S_2^{2-} intermediates, suggests that the intermediates are more likely S_3^{2-} rather than S_2^{2-} species.

Identification of the meta-stable S_x^{2-} species via rotating ring disk electrode measurements.—Another approach to resolve the nature of the S_x^{2-} species is to determine the number of electrons involved in the S_4^{2-} reduction process. Here, we employ the rotating ring disk electrode (RRDE) technique to quantify the electrons transferred during S_4^{2-} reduction by means of a Koutecky-Levich analysis in order to determine the product of the S_4^{2-} reduction. For this, we prepared 4 mM nominal "Li₂S₄" solution in DOL:DME (1:1, v:v) with 1 M LiTFSI by mixing the appropriate amounts of Li₂S and elemental S₈. To ensure that S_4^{2-} is sufficiently stable in DOL:DME-based electrolyte within the time scale of an RRDE experiment (hours), we examined the stability of S_4^{2-} using UV–vis spectroscopy and observed no significant spectroscopic changes over a period of ∼24 h (see section 3.5 in the SI, Fig. S7).

In the RRDE measurements, the potential was negatively scanned until 1.4 V_{Li} (corresponding to −1.9 V_{Fc}) in order to reduce S_4^{2-} and scanned positively only up to 2.4 V_{Li} (−0.85 V_{Fc}) to prevent the oxidation of S_4^{2-} to S₈, which would interfere in subsequent measurements. At the lowest rotation rate of 200 rpm a single diffusion limited current density plateau is obtained; at higher rotation rates, the limiting current density plateau is not reached, but there is clearly no transition to a different number of exchanged electrones observed (see Fig. 5b). From this, the number of electrons (n) transferred in the electrochemical reaction can be determined using a Levich-Koutecky plot of $\frac{1}{i}$ vs ω^{-1} (ω being the RRDE rotation rate in units of rad s⁻¹), as shown in Eq. 26 and Fig. 5c.

$$\frac{1}{i} = \left(\frac{1}{i_k}\right) + \left(\frac{1}{0.62 \cdot n \cdot F \cdot D^{2/3} \cdot \upsilon^{-1/6} \cdot c}\right) \cdot \omega^{-1/2} \qquad [26]$$

Here, n is the number of exchanged electrons, F is Faraday′s constant (96485 A·s·mol⁻¹), c is the "S_4^{2-}" concentration, v is the electrolyte kinematic viscosity, D is the diffusion coefficient of "S_4^{2-}," i is the measured current density, and i_k is the kinetic current density. For known viscosity and diffusion coefficient, the number of exchanged electrons can be quantified. The viscosity was measured with a rheometer (0.014 cm² s⁻¹) and the diffusion coefficient D (7.0 × 10⁻⁶ cm² s⁻¹) was obtained through disk-potential stepping experiments. The experiment details and the comparison of D obtained in this study with the literature are discussed in section of 1.2 of the SI. Based on the Levich-Koutecky correlation (Eq. 26, Fig. 5c), the number of electrons passed during S_4^{2-} reduction is determined to be ∼0.9 ± 0.25 e⁻/S_4^{2-}, which is reasonably close to the expected 0.67 e⁻/S_4^{2-} when S_3^{2-} would be the reduction product (see Eq. 24) and quite different from the 2 e⁻/S_4^{2-} when S_2^{2-} would be the reduction product (Eq. 22).

Both Levich-Koutecky analysis and coulomb ratio analysis of $\frac{Q(\text{region IV})}{Q(\text{region III})}$ suggest that S_3^{2-}, rather than S_2^{2-}, is likely the product of S_4^{2-} reduction. We therefore assign the unknown absorption at ∼266 nm in UV–vis spectrum in DOL:DME-based electrolyte to S_3^{2-}.

Zou and Lu[10] as well as Kim and Park[35] have proposed S_3^{2-} to be the reduction product of $S_3^{\cdot-}$ in DMSO (a high donor number solvent), and ascribed the UV–vis absorption feature at ∼270 nm to S_3^{2-}, which closely coincides with our assignment of the absorption at ∼266 nm to S_3^{2-} in DOL:DME-based electrolyte (both low donor number solvents). Moreover, Assary et al.[54] have computed the energetics of disproportionation and association reactions of poly-sulfide molecular clusters as well as their likely intermediates, based on which they suggested that S_3^{2-} would be the most abundant

intermediate after the complete reductive consumption of S_8^{2-} in solvents such as water, DMSO, ACN, and acetone.[54] Therefore, our hypothesis that S_3^{2-} (~266 nm) is the major liquid intermediate at the 2nd discharge plateau in DOL:DME-based electrolytes seems consistent with our analysis and the above discussed literature.

Probing the reaction pathways of S_3^{2-} formation and depletion.—In the following, we want to probe the formation and depletion reactions of S_3^{2-} in order to better understand the discharge mechanism of Li-S batteries in DOL:DME-based electrolytes.

Formation of S_3^{2-}: The formation of S_3^{2-} in high donor number solvents has so far always been proposed to originate from $S_3^{\cdot -}$

reduction (see. Eq. 17).[10,20,23,35] Yet, in our *operando* UV–vis experiments with DOL:DME (see Figs. 3 and 4) we observed no detectable concentration of $S_3^{\cdot -}$ at/near its absorption at ~618 nm reported for DMSO. Based on the molar absorptivity of $S_3^{\cdot -}$ at ~618 nm in DMSO (~4500 l·mol^{-1}·cm^{-1})[21] and assuming that an absorbance of 0.02 is the detection limit for our *operando* UV–vis cell experiments, the maximum concentration of $S_3^{\cdot -}$ in our experiments must be <0.1 mM. Therefore, the rapid increase of the absorption at ~266 nm in the transition region (see region III in Fig. 4f) which we ascribe to the formation of S_3^{2-} cannot be caused by the reduction of $S_3^{\cdot -}$. Furthermore, our *ex situ* UV–vis analysis of "Li$_2$S$_4$" dissolved in DOL:DME-based electrolyte demonstrates the long-term stability of S_4^{2-} in this electrolyte (see Fig. S7 in section
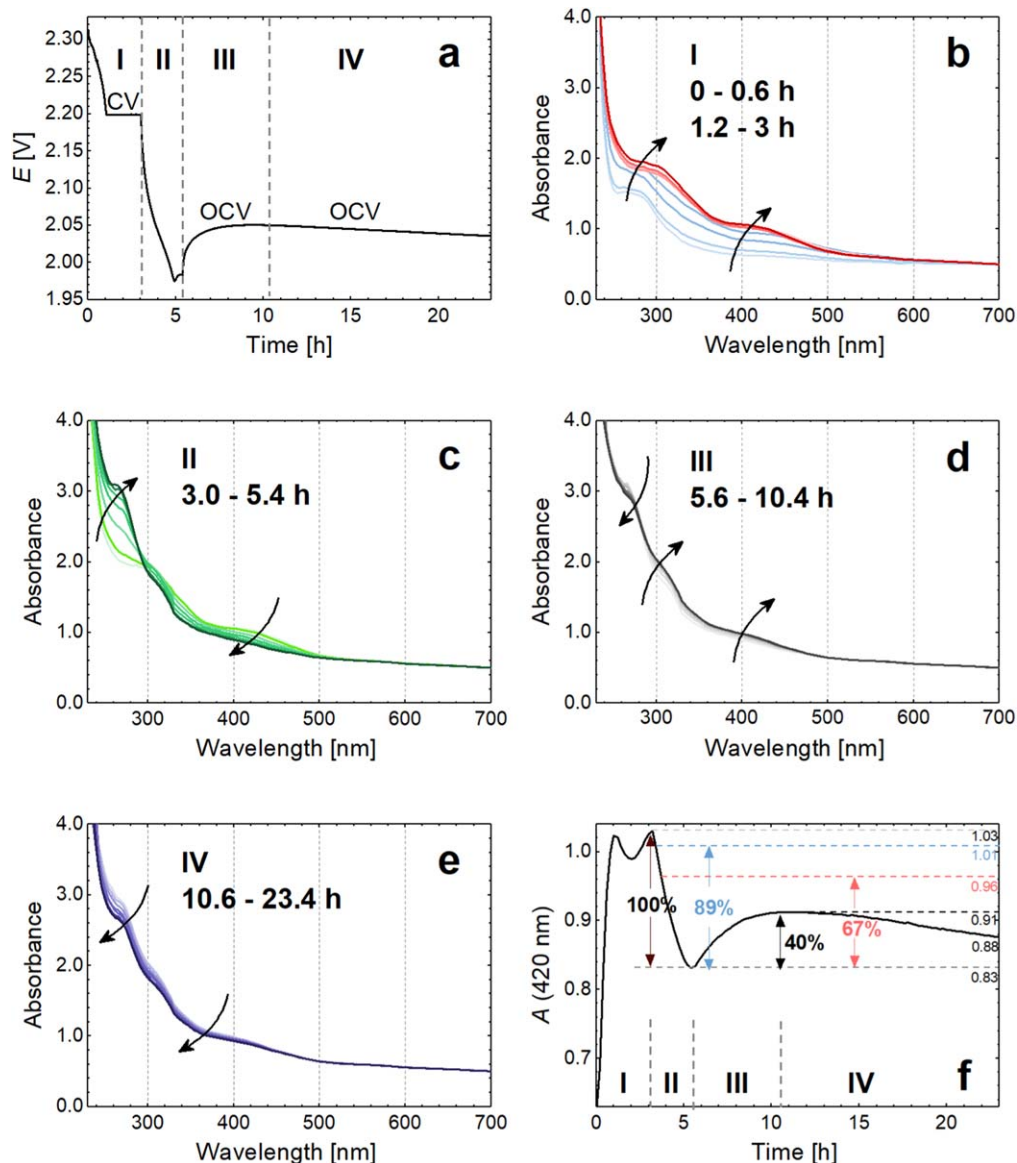
Figure 6. *Operando* UV–vis spectra for a CC discharge at 0.05 h^{-1} C-rate with a 2 h CV hold at the end of the 1st discharge plateau (region I), followed by a CC discharge at 0.05 h^{-1} into the onset of the 2nd discharge plateau (region II), and a final open circuit voltage (OCV) phase at the end of the transition region into the 2nd discharge plateau (regions III & IV) (referred to as "CC-CV-CC-OCV"). (a) Discharge voltage vs time of the *operando* UV–vis cell with an S$_8$/C cathode (0.16 mAh cm^{-2}), a graphite anode pre-lithiated to 50% SOC (~0.22 mAh cm^{-2} delithiation capacity), four separators (Celgard H2013), and 200 μl of DOL: DME (1:1, v:v) with 1 M LiTFSI and 0.1 M LiNO$_3$. The *operando* UV–vis spectra are shown for four different voltage regions: (b) for the 1st discharge plateau and the subsequent CV hold (I; first four spectra were taken every~0.2 h (in blue color) and subsequent spectra every ~0.6 h (in red color)); (c) for the CC discharge during the transition from the 1st to the 2nd discharge plateau (II; one spectrum every ~0.4 h); (d) during the initial OCV phase at the onset of the 2nd discharge plateau (III; one spectrum every ~0.8 h); and, (e) at later stages of the OCV phase (IV; one spectrum every ~2 h). (f) Evolution of the baseline corrected absorption at 420 nm for the voltage profile shown in panel (a); the numbers in percent represent the change of A(420 nm) referenced to the initial decrease of A(420 nm) in region II, where the 67% (blue dashed line) and 89% (pink dashed line) mark the guidelines for A(420 nm) change, when S$_2^{2-}$ or S$_1^{2-}$ would be the product of S$_3^{2-}$ disproportionation reaction, respectively.

of 3.5 of the SI), suggesting that S_3^{2-} cannot either be produced from the self-disproportionation of S_4^{2-} (acc. to Eq. 5). Therefore, we believe that S_3^{2-} is mainly produced by the electrochemical reduction of S_4^{2-} (Eq. 24).

Depletion of S_3^{2-}: In principle, two possible reaction pathways can be postulated for S_3^{2-} depletion, viz., by its electrochemical reduction or by a chemical disproportionation reaction. Since Li_2S was reported to be detected already at the beginning of 2nd discharge plateau through *operando* XRD[31] and XANES,[7] a direct reduction of S_3^{2-} to Li_2S (Eq. 27) would be a reasonable assumption.
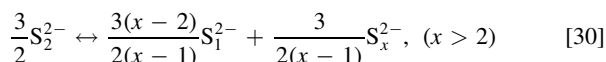
$$S_3^{2-} + 4e^- \rightarrow 3S_1^{2-} \quad [27]$$

However, an analysis of the absorbance at $\sim$266 nm suggests that Eq. 27 is unlikely the only pathway for S_3^{2-} reduction to the final S_1^{2-} product (see section 3.6 of the SI). Apart from its direct electro-chemical reduction to S_1^{2-} (Eq. 27), S_3^{2-} could also first be reduced electrochemically to S_2^{2-} (Eq. 28),

$$S_3^{2-} + 1e^- \rightarrow \frac{3}{2}S_2^{2-} \quad [28]$$

followed either by a subsequent electrochemical reduction reaction (Eq. 29)

$$\frac{3}{2}S_2^{2-} + 3e^- \rightarrow 3S_1^{2-} \quad [29]$$
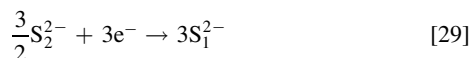
or by a disproportionation reaction (Eq. 30)

$$\frac{3}{2}S_2^{2-} \leftrightarrow \frac{3(x-2)}{2(x-1)}S_1^{2-} + \frac{3}{2(x-1)}S_x^{2-}, \ (x > 2) \quad [30]$$

Unfortunately, a more detailed discussion of Eqs. 28–30 is beyond the scope of this study, as S_2^{2-} cannot be detected by UV–vis spectroscopy and as there is insufficient information about S_2^{2-} in the literature.

To investigate whether S_3^{2-} can be depleted through chemical disproportionation reactions, we examined its stability over time using UV–vis spectroscopy. Here, we electrochemically produce S_3^{2-} in situ in the *operando* cell and monitor it over a subsequent extended OCV period by UV–vis spectroscopy. In order to do so, we adopted the cycling procedure from Fig. 4a until the beginning of the second discharge plateau to achieve a maximal concentration of S_3^{2-} (i.e., progressing through regions I-III in Fig. 4a) and then kept the cell at OCV for about 18 h, as is shown in Fig. 6a (furtheron referred to as CC-CV-CC-OCV procedure). As expected, the absorption at $\sim$266 nm (predominantly from S_3^{2-}, as both S_8 and S_4^{2-} are negligible at the beginning of the 2nd discharge plateau, see Fig. 4f) reaches its maximum at the beginning of the 2nd discharge plateau (see end of region II in Fig. 6c), while the absorption at $\sim$420 nm (from S_4^{2-}) drops to very low values. In the subsequent OCV phase, we observe an increase of A(420 nm) and A(300 nm) in the first 5 h (region III, Fig. 6d), followed by a gradual decrease of A(266 nm), A(300 nm) and A(420 nm) in the 13 h following this initial OCV period (region IV, Fig. 6e). The evolution of A(420 nm) is plotted in Fig. 6f: referenced to the initial decrease of A(420 nm) in region II, its increase in region III would correspond to $\sim$40%, as shown in Fig. 6f. Here is to note that the increase of S_4^{2-} within 5 h is unlikely originated from the residual S_4^{2-} outside of the electrode diffusing back into the slit, as the diffusion time is estimated to be $\sim$10 h based on the shortest diffusion path 5 mm (from electrode perimeter to the edge (in the direction of length) of inner slit) and the measured diffusion coefficient of 7.0×10^{-6} cm^2 s^{-1}.

This 40% increase in the initial $\sim$5 h OCV phase at the onset of the 2nd discharge plateau (region III in Fig. 6) is quite significant and that suggests that S_4^{2-} is gradually regenerated from S_3^{2-} during the OCV phase by chemical disproportionation reactions (see Eqs. 31 and 32).

$$\frac{4}{3}S_3^{2-} \leftrightarrow \frac{2}{3}S_2^{2-}(\text{reduced}) + \frac{2}{3}S_4^{2-}(\text{oxidized}) \quad [31]$$

$$\frac{4}{3}S_3^{2-} \leftrightarrow \frac{4}{9}S_1^{2-}(\text{reduced}) + \frac{8}{9}S_4^{2-}(\text{oxidized}) \quad [32]$$
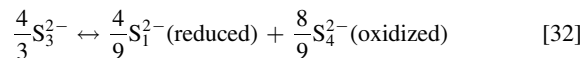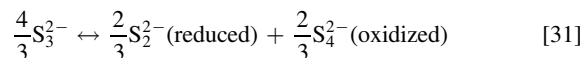
It should be noted here, that no significant decrease of A($\sim$266 nm) is observed in region III (s. Fig. 3d) where S_3^{2-} would be consumed by its disproportionation to S_4^{2-} (Eqs. 30 and 31)). This can be rationalized by the regeneration of S_4^{2-}, which in turn, can compensate the decreased absorption at $\sim$266 nm. (see Fig. 2a or Fig. S7).

This disproportionation reaction verifies the thermodynamic instability of S_3^{2-} in DOL:DME-based electrolytes, which is also in good agreement with the fact that S_3^{2-} ($\sim$266 nm) is not observed in the reference spectra (Fig. 2a) and that it is likely not possible to detect S_3^{2-} in the commonly conducted *ex situ* experiments reported in the literature.[9]

To gain a deeper insight into the reaction product of S_3^{2-} reduction, especially, to address whether Li_2S_2 (Eq. 31) or Li_2S (Eq. 32) can be excluded as the product of S_3^{2-} reduction, a semi-quantitative estimation can be performed. Assuming complete conversion of S_4^{2-} via a first electrochemical reduction step (Eq. 24) and a subsequent disproportionation reaction (Eqs. 31 and 32), a maximum of $\sim$67% (Eq. 31) or $\sim$89% (Eq. 32) of S_4^{2-} can be regenerated back from the assumed initial 100% S_4^{2-} conversion (Eq. 23) in the transition region. If the possible regeneration of S_4^{2-} through S_3^{2-} disproportionation were higher than $\sim$67%, it would then suggest S_1^{2-}, rather than S_2^{2-}, is the reduction product. Therefore we try to estimate the maximal amount of S_4^{2-} that can be regenerated from the S_3^{2-} disproportionation.

At the same time, we also observe a very slow but noticeable decrease of the absorption between 250 and $\sim$500 nm over the last 13 h of the OCV period (region IV, Fig. 6e). This can be rationalized by 1) the existing polysulfides diffusing out of the electrode over this extend OCV period and 2) a continuous depletion of polysulfide species on the graphite anode on account of an imperfect SEI.

We assume this slow consumption of polysulfides in region IV would also occur in region III, so that this needs to be included in the estimate of the maximal regeneration of the S_4^{2-} concentration in region III. For a rough estimate, the decrease of A(420 nm) between 13–23 h in Fig. 6f can be linearized, yielding a constant A(420 nm) signal loss rate:

$$c = \frac{\Delta A}{\Delta t} = \frac{A_{13h}(420\,\text{nm}) - A_{23h}(420\,\text{nm})}{10\,\text{h}} = 0.003\,h^{-1} \quad [33]$$

With this estimated A(420 nm) signal loss rate, we can now project the loss of the A(420 nm) signal over the course of the initial OCV period (region III) that is caused by the loss of dissolved polysulfides through its diffusion and the slow but continuous reaction with the lithiated graphite counter electrode:

$$\Delta A_{5.6-10.4\,h}(420\,\text{nm}) = c^*\Delta t = 0.003\,\text{h}^{-1*}\,4.8\,\text{h} = 0.014 \quad [34]$$

Adding this value to the (local) maximum of the A(420 nm) signal at 10.4 h (see Fig. 6f), we obtain a maximum A(420 nm) value in the initial OCV period of $\sim$0.92 (from 0.014 + 0.91), which is about 47% of the decrease of the A(420 nm) signal in region II that is caused by the electrochemical reduction of S_4^{2-} to S_3^{2-} in the transition region.

The estimated increase of $\sim$47% is lower than both maximum value of $\sim$67% and of $\sim$89%, so that we can exclude neither Li_2S_2 (Eq. 31) nor Li_2S (Eq. 32) as the reduced species upon dispropor-tionation of S_3^{2-}.

Proposed discharge mechanism of Li-S batteries in DOL:DME-based electrolyte.—Figure 7 summarizes the reaction intermediates
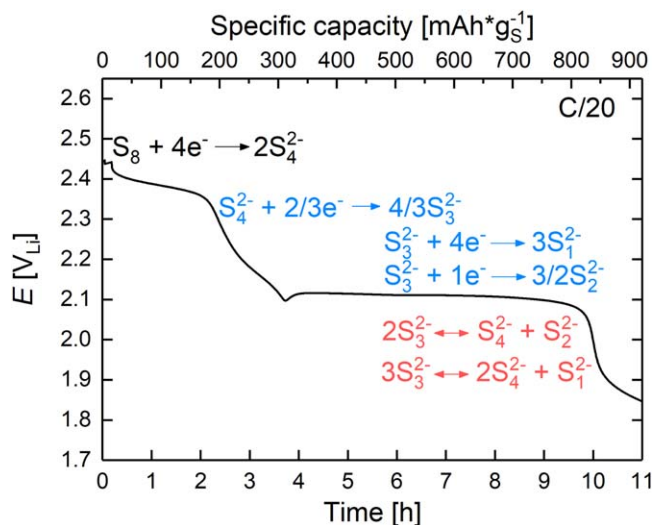
Figure 7. Proposed discharge mechanism of Li-S batteries in DOL:DME-based electrolyte. The relevant electrochemical steps deduced in this study are presented in blue and the disproportionation reactions are presented in red. The exemplary voltage profile (black solid line) is taken from Fig. 1b (blue line).

deduced from our above presented *operando* transmission UV–vis spectroscopy experiments. Based on the proposed discharge reaction pathways, the ratio of coulombic charge delivered at different regions during the discharge would be expected to be as follows:

$$Q(1^{st} \text{ plateau}): Q(\text{transition region}): Q(2^{nd} \text{ plateau})$$
$$= 4e^-: \frac{4}{3}e^-: \frac{32}{3}e^- = 3: 1: 8 \qquad [35]$$

However, the ratio of $Q(2^{nd}$ plateau$):Q$(transition region) would always be smaller than $= 8:1$, since i) the formed S_3^{2-} in the transition region can relatively fast disproportionate to S_4^{2-}, contributing to Q(transition region), and ii) the conversion of S_3^{2-} to Li_2S seems to be limiting ($<100\%$ conversion), which would shorten the 2nd discharge plateau.

Like many other research works investigating the Li-S chemistry with transmission UV–vis spectroscopy (e.g., 2 mM S_8 in DOL:DME-based electrolyte,[10] 1.2 mM S_8,[36] and 3 mM S_8,[35] in DMSO-based electrolyte, 2.5 mM S_8 in DMF-based-electrolyte[37]), these low concentrations of sulfur and of the resulting polysulfides are required for UV–vis studies due to the high molar absorptivities of these species. While the relative abundance of the various polysulfides observed in previous studies and in our present study conducted at high E/S ratios may not be in quantitative agreement with that in practical Li-S cells, we do believe that they provide relevant insights into the general speciation in Li-S cells. The mechanistic insights gained in *operando* UV–vis cells restricted to operate at high E/S ratios should still provide further understanding about possible reaction steps and species in the S-redox reactions. Especially, the *operando* UV–vis cell in this study may even present a quite viable, if not the major, reaction pathway of how S_8 is electrochemically discharged to Li_2S_2/Li_2S, as demonstrated by its reasonable discharge voltage profile and discharge capacity, which fairly well resembles those obtained with conventional Li-S cells with high sulfur loadings and low E/S ratios.[11,48]

Conclusions

In this study, we introduce an *operando* transmission UV–vis spectro-electrochemical cell design that is suitable for mechanistic studies of cell chemistries involving soluble chromophoric intermediates, e.g., polysulfides in Li-S batteries.

We accomplish a systematic UV–vis spectroscopic peak assignment for polysulfides in DOL:DME-based electrolyte and, for the first time, we are able to identify and distinguish the liquid intermediates (S_8 and different polysulfides) during the first discharge of a Li-S battery. We show that elemental S_8 is converted to S_4^{2-} during the 1st discharge plateau where other polysulfides are barely detected. The formed S_4^{2-} gets reduced to a meta-stable polysulfide species in the transition region between the two discharge plateaus that dominates the UV–vis spectra over the course of the 2nd discharge plateau. We identify this meta-stable polysulfide as S_3^{2-} via an analysis of the transferred charges and the formed species in the *operando* cell as well as via the number of electrons transferred for S_4^{2-} reduction using the rotating ring disk electrode technique. We show that S_3^{2-} is a meta-stable species that rather quickly disproportionates to S_4^{2-} and Li_2S_2/Li_2S, so that it is difficult to detect in *ex situ* samples/experiments. Our study suggests that the conversion of S_8 to S_4^{2-} and then to S_3^{2-} are fast processes, while the capacity extraction from S_3^{2-} to form Li_2S is limiting the discharge rate in DOL:DME-based Li-S batteries.

ORCID

Qi He https://orcid.org/0000-0002-2174-8187

References

1. J. Conder, R. Bouchet, S. Trabesinger, C. Marino, L. Gubler, and C. Villevieille, *Nat. Energy*, **2**, 17069 (2017).
2. M. Barghamadi, A. S. Best, A. I. Bhatt, A. F. Hollenkamp, M. Musameh, R. J. Rees, and T. Rüther, *Energy Environ. Sci.*, **7**, 3902 (2014).
3. S. Zhang, K. Ueno, K. Dokko, and M. Watanabe, *Adv. Energy Mater.*, **5**, 1500117 (2015).
4. D. Eroglu, K. R. Zavadil, and K. G. Gallagher, *J. Electrochem. Soc.*, **162**, A982 (2015).
5. L. Cheng, L. A. Curtiss, K. R. Zavadil, A. A. Gewirth, Y. Shao, and K. G. Gallagher, *ACS Energy Lett.*, **1**, 503 (2016).
6. Y.-C. Lu, Q. He, and H. A. Gasteiger, *J. Phys. Chem. C*, **118**, 5733 (2014).
7. Y. Gorlin, A. Siebel, M. Piana, T. Huthwelker, H. Jha, G. Monsch, F. Kraus, H. A. Gasteiger, and M. Tromp, *J. Electrochem. Soc.*, **162**, A1146 (2015).
8. Y. Gorlin, M. U. M. Patel, A. Freiberg, Q. He, M. Piana, M. Tromp, and H. A. Gasteiger, *J. Electrochem. Soc.*, **163**, A930 (2016).
9. C. Barchasz, F. Molton, C. Duboc, J. C. Leprêtre, S. Patoux, and F. Alloin, *Anal. Chem.*, **84**, 3973 (2012).
10. Q. Zou and Y.-C. Lu, *J. Phys. Chem. Lett.*, **7**, 1518 (2016).
11. T. Poux, P. Novák, and S. Trabesinger, *J. Electrochem. Soc.*, **163**, A1139 (2016).
12. H. Wang, N. Sa, M. He, X. Liang, L. F. Nazar, M. Balasubramanian, K. G. Gallagher, and B. Key, *J. Phys. Chem. C*, **121**, 6011 (2017).
13. M. Cuisinier, P.-E. Cabelguen, S. Evers, G. He, M. Kolbeck, A. Garsuch, T. Bolin, M. Balasubramanian, and L. F. Nazar, *J. Phys. Chem. Lett.*, **4**, 3227 (2013).
14. A. Manthiram, Y. Fu, S. Chung, C. Zu, and Y. Su, *Chem. Rev.*, **114**, 11751 (2014).
15. Y. V. Mikhaylik and J. R. Akridge, *J. Electrochem. Soc.*, **151**, A1969 (2004).
16. M. Wild, L. O'Neill, T. Zhang, R. Purkayastha, G. Minton, M. Marinescu, and G. J. Offer, *Energy Environ. Sci.*, **8**, 3477 (2015).
17. Q. He, Y. Gorlin, M. U. M. Patel, H. A. Gasteiger, and Y.-C. Lu, *J. Electrochem. Soc.*, **165**, A4027 (2018).
18. A. T. S. Freiberg, A. Siebel, A. Berger, S. M. Webb, Y. Gorlin, M. Tromp, and H. A. Gasteiger, *J. Phys. Chem. C*, **122**, 5303 (2018).
19. S. D. Talian, J. Moskon, R. Dominko, M. Gaberscek, S. D. Talian, J. Moškon, R. Dominko, and M. Gaberšček, *Appl. Mater. Interfaces*, **9**, 29760 (2017).
20. M. Cuisinier, C. Hart, M. Balasubramanian, A. Garsuch, and L. F. Nazar, *Adv. Energy Mater.*, **5**, 1401801 (2015).
21. R. P. Martin, W. H. Doub, J. L. Roberts, and D. T. Sawyer, *Inorg. Chem.*, **12**, 1921 (1973).
22. H. Yamin, A. Gorenshtein, J. Penciner, Y. Sternberg, and E. Peled, *J. Electrochem. Soc.*, **135**, 1045 (1988).
23. J. Paris and V. Plichon, *Electrochim. Acta*, **26**, 1823 (1981).
24. M. U. M. Patel and R. Dominko, *ChemSusChem*, **7**, 2167 (2014).

25. G. Bieker, J. Wellmann, M. Kolek, K. Jalkanen, M. Winter, and P. M. Bieker, *Phys. Chem. Chem. Phys.*, **19**, 11152 (2017).
26. T. Chivers and P. J. W. Elder, *Chem. Soc. Rev.*, **42**, 5996 (2013).
27. Y. V. Mikhaylik and J. R. Akridge, *J. Electrochem. Soc.*, **150**, A306 (2003).
28. A. Evans, M. I. Montenegro, and D. Pletcher, *Electrochem. Commun.*, **3**, 514 (2001).
29. J. D. Mcbrayer, T. E. Beechem, B. R. Perdue, C. A. Apblett, and F. H. Garzon, *J. Electrochem. Soc.*, **165**, A876 (2018).
30. N. Saqib, G. M. Ohlhausen, and J. M. Porter, *J. Power Sources*, **364**, 266 (2017).
31. S. Waluś, C. Barchasz, R. Bouchet, J.-C. Leprêtre, J.-F. Colin, J.-F. Martin, E. Elkaïm, C. Baehtz, and F. Alloin, *Adv. Energy Mater.*, **5**, 1500165 (2015).
32. H. Jha, I. Buchberger, X. Cui, S. Meini, and H. A. Gasteiger, *J. Electrochem. Soc.*, **162**, A1829 (2015).
33. N. A. Cañas, D. N. Fronczek, N. Wagner, A. Latz, and K. A. Friedrich, *J. Phys. Chem. C*, **118**, 12106 (2014).
34. D.-H. Han, B.-S. Kim, S.-J. Choi, Y. Jung, J. Kwak, and S.-M. Park, *J. Electrochem. Soc.*, **151**, E283 (2004).
35. B.-S. Kim and S.-M. Park, *J. Electrochem. Soc.*, **140**, 115 (1993).
36. R. Bonnaterre and G. Cauquis, *J. Chem. Soc., Chem. Commun.*, **0**, 293 (1972).
37. F. Gaillard and E. Levillain, *J. Electroanal. Chem.*, **398**, 77 (1995).
38. F. Gaillard, E. Levillain, and J. P. Lelieur, *J. Electroanal. Chem.*, **432**, 129 (1997).
39. P. Leghié, J. Lelieur, and E. Levillain, *Electrochem. Commun.*, **4**, 628 (2002).
40. E. Levillain, F. Gaillard, P. Leghie, A. Demortier, and J. P. Lelieur, *J. Electroanal. Chem.*, **420**, 167 (1997).
41. H. Jha and H. A. Gasteiger, *DE Pat. No. 102013005082 A1. Munich, Germany*, Deutsches Patent- und Markenamt (2014).
42. R. D. Rauh, F. S. Shuker, J. M. Marston, and S. B. Brummer, *J. Inorg. Nucl. Chem.*, **39**, 1761 (1977).
43. J. Herranz, A. Garsuch, and H. A. Gasteiger, *J. Phys. Chem. C*, **116**, 19084 (2012).
44. F. Y. Fan and Y. Chiang, *J. Electrochem. Soc.*, **164**, A917 (2017).
45. M. Hagen, D. Hanselmann, K. Ahlbrecht, R. Maça, D. Gerber, and J. Tübke, *Adv. Energy Mater.*, **5**, 1401986 (2015).
46. S.-H. Chung and A. Manthiram, *ACS Energy Lett.*, **2**, 1056 (2017).
47. A. Rosenman, R. Elazari, G. Salitra, E. Markevich, D. Aurbach, and A. Garsuch, *J. Electrochem. Soc.*, **162**, A470 (2015).
48. M. Hagen, P. Fanz, and J. Tübke, *J. Power Sources*, **264**, 30 (2014).
49. A. Kawase, S. Shirai, Y. Yamoto, R. Arakawa, and T. Takata, *Phys. Chem. Chem. Phys.*, **16**, 9344 (2014).
50. P. Leghi, J. Lelieur, and E. Levillain, *Electrochem. Commun.*, **4**, 406 (2002).
51. N. S. A. Manan, L. Aldous, Y. Alias, P. Murray, L. J. Yellowlees, M. C. Lagunas, and C. Hardacre, *J. Phys. Chem. B*, **115**, 13873 (2011).
52. C. Reichardt, *Chem. Rev.*, **94**, 2319 (1994).
53. H.-H. Perkampus, *UV-VIS Spectroscopy and its Applications* (Springer, Berlin Heidelberg) (1992).
54. R. S. Assary, L. A. Curtiss, and J. S. Moore, *J. Phys. Chem. C*, **118**, 11545 (2014).
55. Z. Feng, C. Kim, A. Vijh, M. Armand, K. H. Bevan, and K. Zaghib, *J. Power Sources*, **272**, 518 (2014).
56. M. Helen, M. A. Reddy, T. Diemant, U. Golla-Schindler, R. J. Behm, U. Kaiser, and M. Fichtner, *Sci. Rep.*, **5**, 12146 (2015).
57. T. A. Pascal, K. H. Wujcik, R. Wang, P. Balsara, and D. Prendergast, *Phys. Chem. Chem. Phys.*, **19**, 1441 (2017).
58. T. Fujinaga, T. Kuwamoto, S. Okazaki, and M. Hojo, *Bull. Chem. Soc. Jpn.*, **53**, 2851 (1980).
59. A. J. Bard and L. R. Faulkner, *Electrochemical Methods Fundamentals and Applications* (John Wiley & Sons, INC, New York, NY) 2nd ed. (2000).